Supporting Information

Robust Aluminium and Iron Phosphinate Metal Organic Frameworks for Efficient Removal of Bisphenol A

*Daniel Bůžek,[a,b] Soňa Ondrušová,[a] Jan Hynek,[a] Petr Kovář,[c] Kamil Lang,[a] Jan Rohlíček,[d] Jan Demel[a]**

[a] Institute of Inorganic Chemistry of the Czech Academy of Sciences, 250 68 Řež, Czech Republic; E-mail: demel@iic.cas.cz

[b] Faculty of the Environment, Jan Evangelista Purkyně University, Králova Výšina 3132/7, 400 96 Ústí nad Labem, Czech Republic

[c] Charles University, Faculty of Mathematics and Physics, Ke Karlovu 3, 121 16, Praha 2, Czech Republic

[d] Institute of Physics of the Czech Academy of Sciences, 182 21 Praha, Czech Republic

Table of content

Experimental procedures

Table S1	Elemental analysis of ICR MOFs.
Figures S1-S7	FTIR spectra of ICR MOFs.
Figures S8-S14	TGA/DTA curves and the evolution of gases for ICR MOFs.
Table S2	Crystallographic data.
Figures S15-S18	Rietveld fits of Fe-ICR-5, Fe-ICR-6, Fe-ICR-7, and Al-ICR-4.
Figure S19	Comparison of crystal structure of Fe-ICR-3 and Fe-ICR-5.
Figure S20	Comparison of PXRD patterns of Al- and Fe-ICR MOFs.
Figures S21-24	Pore size distributions of all ICR MOFs.
Figures S25-S42	PXRD of ICR MOFs after treatment in H_2O, EtOH, toluene, and activation from water.
Figure S43	Nitrogen adsorption isotherms of as-prepared Al-ICR-2, Al-ICR-4, Al-ICR-6, and Al-ICR-7.
Figures S44-S61	Nitrogen adsorption isotherms of ICR MOFs after treatment in H_2O, EtOH, toluene, and activation from water.

Equations used for the analysis of adsorption properties of ICR MOFs.

Figure S62	Kinetic curves of BPA adsorption.
Figure S63	Non-linear fitting of BPA adsorption isotherms.
Table S3	Langmuir, Freundlich, and Langmuir-Freundlich parameters.
Figure S64	PXRD patterns of Al-ICR MOFs before and after adsorption of BPA.
Table S4	BET surface area of Al-ICR MOFs before and after adsorption of BPA.

Details of molecular modelling.

Figure S65	Arrangement of BPA inside the Al-ICR-6 pores.
Figure S66	Arrangement of BPA molecules with a loading of 300 mg g^{-1} in the pores of Al-ICR-6 and Al-ICR-7.

Experimental Procedures

Materials. $MePCl_2$ (Acros Organics), $AlCl_3 \cdot 6H_2O$, *N,N*-dimethylformamide (DMF) (both Penta, Czech Republic), benzene (anhydrous), $PhPCl_2$, 1,4-dibromobenzene, 4,4′-dibromobiphenyl, activated charcoal (AC), $Pd(PPh_3)_4$, $FeCl_3 \cdot 6H_2O$ (all Sigma-Aldrich), ethanol (absolute, Fischer Chemical), were used as purchased. 1,4-dioxane (water-free, VWR Chemicals), dichloromethane (HPLC grade, Fisher Scientific), and methanol (anhydrous, VWR Chemicals) were dried using a solvent purifier SP-1 (LC Technology Solutions). Triethylamine (Sigma-Aldrich) was freshly distilled from Na under Ar. Acetonitrile (Lach-Ner, Czech Republic) was dried using molecular sieves (3 Å, Sigma Aldrich). The synthesis of linkers was performed under Ar using standard Schlenk technique. Column chromatography was performed on Sigma-Aldrich 60 (70-230 mesh, 60 Å) silica gel.

Preparation of linker molecules

General procedure for preparation of methyl R-phosphinates. A Schlenk tube was charged with $RPCl_2$, three times evacuated and flushed with Ar, and diluted with dry benzene (8 mL per 1 g of $RPCl_2$). In a second Schlenk tube, 2.4 molar equivalents of dry MeOH were mixed with 1 molar equivalent of dry triethylamine under Ar atmosphere. The mixture was cooled by an ice bath and the solution of $RPCl_2$ was slowly added. The formed precipitate was filtered off and the filtrate was evaporated yielding an oily product which was directly used without any purification for further synthesis.

Methyl methylphospinate.
Yield: 5.17 g (64 %).
^{1}H NMR ($CDCl_3$): δ 1.55 (d, $^2J_{PH}$ = 15.6 Hz, 3H); 3.78 (d, $^3J_{PH}$ = 12.0 Hz, 3H); 7.19 (d, $^1J_{PH}$ = 540 Hz, 1H). $^{31}P\{^1H\}$ NMR ($CDCl_3$): δ 37.51.

Methyl phenylphospinate.
Yield: 10.7 g (80 %).
^{1}H NMR ($CDCl_3$): δ 3.78 (d, $^3J_{PH}$ = 12.3 Hz, 3H); 7.49 – 7.53 (m, 2H); 7.55 (d, $^1J_{PH}$ = 566 Hz, 1H); 7.58 – 7.62 (m, 1H); 7.75 – 7.80 (m, 2H). $^{31}P\{^1H\}$ NMR ($CDCl_3$): δ 27.75.

General procedure for preparation of dimethyl arylene bis(R-phosphinates). A flask was charged with dibromoarene and 0.16 molar equivalents of $Pd(PPh_3)_4$, three times evacuated and flushed with Ar, and sealed with a septum. Then, 2.4 molar equivalents of dry

triethylamine and 3 molar equivalents of methyl or phenyl phosphinate were dissolved in dry 1,4-dioxane under Ar atmosphere, and added to the dibromoarene mixture. The resulting yellow solution was stirred at 60 °C for 96 h. After cooling down, the formed precipitate was filtered off and the filtrate was evaporated to dryness. The solid residue was dissolved in dichloromethane and washed three times with water. The purification process was individual for each product, see below.

Dimethyl phenylene-1,4-bis(methylphosphinate). The mixed water fractions were evaporated to dryness. The obtained mixture of the desired product with residual triethylamine hydrobromide was used for the following synthetic step without any further purification. Yield 5.12 g (82 %).
^{1}H NMR ($CDCl_3$): δ 1.55 (d, $^{2}J_{PH}$ = 14.4 Hz, 6H); 3.64 (d, $^{3}J_{PH}$ = 11.2 Hz, 6H); 7.87 – 7.97 (m, 4H). ^{31}P{^{1}H} NMR ($CDCl_3$): δ 43.4.

Dimethyl phenylene-1,4-bis(phenylphosphinate). The organic phase was dried over $MgSO_4$. The solution was evaporated and the product was precipitated by addition of diethyl ether, filtered off, and washed until the filtrate was colourless. Yield: 5.6 g (61 %).
^{1}H NMR ($CDCl_3$): δ 3.75 (d, $^{3}J_{PH}$ = 11.4 Hz, 6H); 7.43 – 7.47 (m, 4H); 7.51 – 7.54 (m, 2H); 7.78 (dd, $^{3}J_{PH}$ = 12.0 Hz, $^{3}J_{HH}$ = 7.8 Hz, 4H); 7.87 (dd, $^{3}J_{PH}$ = 9.0 Hz, $^{3}J_{HH}$ = 6.0 Hz, 4H).
^{31}P{^{1}H} NMR ($CDCl_3$): δ 32.4.

Dimethyl biphenylene-4,4'-bis(methylphosphinate). The organic phase was dried over $MgSO_4$. The solution was evaporated and the product was precipitated by the addition of diethyl ether, filtered off, and washed with diethyl ether and DMF until the filtrate was colourless. Yield: 7.6 g (70 %).
^{1}H NMR ($CDCl_3$): δ 1.55 (d, $^{2}J_{PH}$ = 14.4 Hz, 6H); 3.75 (d, $^{3}J_{PH}$ = 11.6 Hz, 6H); 7.73 (dd, $^{3}J_{PH}$ = 14.8 Hz, $^{3}J_{HH}$ = 7.8 Hz, 4H); 7.84 (dd, $^{4}J_{PH}$ = 10.2 Hz $^{3}J_{HH}$ = 7.8 Hz, 4H). ^{31}P{^{1}H} NMR ($CDCl_3$): δ 44.3.

Dimethyl biphenylene-4,4'-bis(phenylphosphinate). The organic phase was dried over $MgSO_4$. The solution was evaporated and the product was precipitated by the addition of acetonitrile, filtered off, and washed until the filtrate was colourless. Yield: 3.52 g (54 %).
^{1}H NMR ($CDCl_3$): δ 3.79 (d, $^{3}J_{PH}$ = 10.8 Hz, 6H); 7.47 (td, $^{3}J_{HH}$ = 7.8 Hz, $^{4}J_{PH}$ = 3.6 Hz, 4H); 7.54 (t, $^{3}J_{HH}$ = 7.8 Hz, 2H); 7.65 (dd, $^{3}J_{HH}$ = 7.8 Hz, $^{4}J_{PH}$ = 3.0 Hz, 4H); 7.83 (dd, $^{3}J_{PH}$ = 12.6

Hz, $^{3}J_{HH}$ = 7.8 Hz, 4H); 7.88 (dd, $^{3}J_{PH}$ = 12.0 Hz, $^{3}J_{HH}$ = 7.8 Hz, 4H). $^{31}P\{^{1}H\}$ NMR ($CDCl_3$): δ 33.5.

General procedure for preparation of arylene bis(R-phosphinic acids). A Schlenk tube was charged with dimethyl arylene bis(R-phosphinate), evacuated and flushed with argon three times, and then acetonitrile (approx. 40 mL g^{-1}) was added followed by a dropwise addition of 3 molar equivalents of trimethylsilyl bromide. In the case of dimethyl biphenylene-4,4'-bis(phenylphosphinate), dichloromethane was used instead of acetonitrile due to poor solubility of the ester in acetonitrile. The resulting mixture was stirred at 40 °C for 16 h. The purification process was individual for each product, see below.

Phenylene-1,4-bis(methylphosphinic acid) (H_2PBP(Me)). After cooling down the solution was evaporated to dryness. The solid residue was dissolved in water and the water solution was washed with diethyl ether three times. The water fraction was evaporated and the crude product was purified by trituration with acetone. Yield: 10.1 g (66 %).
^{1}H NMR (CD_3OD): δ 1.69 (d, $^{2}J_{PH}$ = 14.4 Hz, 6H); 7.93 – 8.03 (m, 4H). $^{31}P\{^{1}H\}$ NMR (CD_3OD): δ 39.3. $^{13}C\{^{1}H\}$ NMR (CD_3OD): δ 15.1 (d, $^{1}J_{PC}$ = 101 Hz); 130.6 (t, J_{PC} = 12 Hz); 137.7 (d, $^{1}J_{PC}$ = 129 Hz).

Phenylene-1,4-bis(phenylphosphinic acid) (H_2PBP(Ph)). After cooling down, the solution was precipitated by addition of water. The solid product was filtered off and washed with acetonitrile, water, and acetone. Yield: 5.0 g (96 %).
^{1}H NMR ($(CD_3)_2SO$): δ 7.43 (dt, $^{3}J_{HH}$ = 7.2 Hz, $^{4}J_{PH}$ = 3.0 Hz, 4H); 7.50 (t, $^{3}J_{PH}$ = 7.2 Hz, 2H); 7.68 (dd, $^{3}J_{PH}$ = 12.0 Hz, $^{3}J_{HH}$ = 7.2 Hz, 4H); 7.77 (dd, $^{3}J_{PH}$ = 8.4 Hz, $^{3}J_{HH}$ = 6.0 Hz, 4H). $^{31}P\{^{1}H\}$ NMR (CD_3OD): δ 23.1. $^{13}C\{^{1}H\}$ NMR (CD_3OD): δ 129.1 (d, J_{PC} = 13 Hz); 131.4 (t, J_{PC} = 12 Hz); 131.5 (d, J_{PC} = 11 Hz); 132.2 (s); 134.9 (d, $^{1}J_{PC}$ = 135 Hz); 138.7 (d, $^{1}J_{PC}$ = 130 Hz).

Biphenylene-4,4'-bis(methylphosphinic acid) (H_2BBP(Me)). After cooling down, the reaction mixture was evaporated to dryness. The solid residue was suspended in ethanol. The product was filtered off and washed with acetone and diethyl ether. Yield: 6.9 g (99 %).
^{1}H NMR ($(CD_3)_2SO$): δ 1.51 (d, $^{2}J_{PH}$ = 15.0 Hz, 6H); 7.75 – 7.80 (m, 8H). $^{31}P\{^{1}H\}$ NMR ($(CD_3)_2SO$): δ 34.8. $^{13}C\{^{1}H\}$ NMR ($(CD_3)_2SO$): δ 17.4 (d, $^{1}J_{PC}$ = 111 Hz); 127.4 (d, J_{PC} = 12 Hz); 131.7 (d, J_{PC} = 9 Hz); 135.6 (d, $^{1}J_{PC}$ = 127 Hz); 142.6 (s).

Biphenylene-4,4'-bis(phenylphosphinic acid) (H_2BBP(Ph)). After cooling down, the solution was evaporated and the residue was precipitated by the addition of water. The solid product was filtered off and washed with water, acetone, and diethyl ether. Yield: 3.2 g (96 %).

^{1}H NMR ($(CD_3)_2SO$): δ 7.44 (td, $^3J_{HH}$ = 7.2 Hz, $^4J_{PH}$ = 3.0 Hz, 4H); 7.54 (t, $^3J_{HH}$ = 6.6 Hz, 2H); 7.70 – 7.79 (m, 12H). ^{31}P{^{1}H} NMR (CD_3OD): δ 23.7. ^{13}C{^{1}H} NMR ($(CD_3)_2SO$): δ 127.6 (d, J_{PC} = 12 Hz); 129.0 (d, J_{PC} = 12 Hz); 131.5 (s); 132.1 (d; J_{PC} = 9 Hz); 135.0 (d, $^1J_{PC}$ = 135 Hz); 135.4 (d, $^1J_{PC}$ = 135 Hz); 142.5 (s).

Preparation of ICR MOFs

Preparation of Fe-ICR-2, Fe-ICR-4, and Fe-ICR-7. A teflon lined autoclave (Berghof DAB-2) was charged with 0.08 mmol linker and 0.04 mmol $FeCl_3 \cdot 6H_2O$ (10.8 mg) and overlaid with 5 mL of absolute EtOH. The sealed autoclave was heated in a preheated heating mantle (Berghof BTC-3000) at 250 °C for 24 h. The resulting white powder was centrifuged (11,000 rpm, 5 min, Hettich, Rotina 380 R), washed five times with EtOH (third time it was left in EtOH for two hours), three times with water (second time it was left in water overnight), three times with acetone (third time it was left in acetone for 1.5 h), and activated at 80 °C for five hours under dynamic vacuum.

Preparation of Fe-ICR-5. A teflon lined autoclave (Berghof DAB-2) was charged with 0.08 mmol of H_2BBP(Me), 0.04 mmol $FeCl_3 \cdot 6H_2O$ (10.8 mg), and overlaid with 5 mL of absolute EtOH. The sealed autoclave was heated in a preheated heating mantle (Berghof BTC-3000) at 250 °C for 24 h. The resulting white powder was centrifuged (11,000 rpm, 5 min, Hettich, Rotina 380 R), washed five times with acetone, and dried on air.

Preparation of Fe-ICR-6. A Wheaton vial was charged with 37.2 mg H_2BBP(Me) (0.12 mmol) with 25 ml of DMF. After 10 min sonication 0.06 mmol of $FeCl_3 \cdot 6H_2O$ (16.2 mg) in 5 mL of DMF was added. The vial was heated in a preheated oven (Berghof BTC-3000) at 120 °C for 72 h. The resulting white powder was centrifuged (11,000 rpm, 5 min, Hettich, Rotina 380 R) and washed as described above for Fe-ICR-2.

Preparation of Al-ICR-2, Al-ICR-4, Al-ICR-6, and Al-ICR-7. A teflon lined autoclave (Berghof DAB-2) was charged with 0.0425 mmol linker and 0.0213 mmol $AlCl_3 \cdot 6H_2O$ (5.13 mg) and overlaid with 10 mL of absolute EtOH. The sealed autoclave was heated in a

preheated heating mantle (Berghof BTC-3000) at 250 °C for 24 h. The resulting white powder was centrifuged (11,000 rpm, 5 min, Hettich, Rotina 380 R) and washed as described above for Fe-ICR-2.

Stability studies

20 mg of ICR MOF was suspended in 10 mL of water, EtOH, or toluene and the suspension was shaken at RT or refluxed for 24 h. After that, the solid material was collected by centrifugation, washed twice with water (in the case of stability tests in water) or ethanol (in the case of stability tests in ethanol or toluene), and twice with acetone. The resulting powders were air-dried at RT.

Activation from wet suspension was done by suspending 20 mg of ICR MOF in water and letting the water freely evaporate on air at RT.

Sorption of bisphenol A (BPA)

The sorption of BPA was performed in sealed 100 mL SIMAX glass bottles with initial concentrations ranging from 10 to 120 mg L^{-1} in a temperature-controlled room with constant temperature of 25 ± 1 °C. The bottles were charged with 10 mg of Al-ICR MOF or activated charcoal (AC, DARCO®, 100 mesh particle size, powder, Sigma Aldrich) and 10 mL of water, followed by 5 min sonication. Then, 40 mL of BPA solution of the required concentration was added. The mixture was stirred for 24 h at 25 °C and then 1 mL of sample was taken, filtered through a PTFE microfilter (0.2 μm, Whatman), and the equilibrium concentration of BPA was determined using an HPLC-DAD instrument. A set of experiments using different sorption times showed that 24 h ensures the establishing of the equilibrium.

The kinetic experiments were performed using a similar procedure. The initial concentration of BPA was set to 50 mg L^{-1}, 0.3 mL aliquots were taken at predefined times (1 - 360 min) and analysed. All experiments were performed under stirring in the temperature-controlled room at 25 ± 1 °C.

All sorption experiments were performed in water of natural pH without any pH adjustment. The natural pH in all cases was 4.5 ± 0.3. All presented results are average of three independent experiments giving the relative standard deviation lower than 7 %.

The Al-ICR MOFs were regenerated after the sorption of BPA by washing three times with water and three times with acetone. These solid samples were then analysed by PXRD and N_2 adsorption isotherms.

The kinetic and adsorption curves were analysed using a pseudo-second order model and Langmuir, Freundlich, and Langmuir-Freundlich adsorption isotherms (corresponding equations are given below), respectively. The equilibrium points were not used for fitting to the pseudo-second order kinetic model (approximately > 100 min) as recommended in literature.[1]

Instrumental methods

NMR spectra were measured on a JEOL 600 MHz NMR spectrometer. ^{1}H and ^{13}C NMR spectra were referenced on the residual signal of the solvent. CHN elemental analysis was performed using a standard combustion technique (Thermo Scientific FlashSmartTM 2000 Elemental analyzer). Powder X-ray diffractions (PXRD) were recorded using an Empyrean diffractometer (PANalytical), which was equipped by a capillary holder, focusing mirror and PIXcel3D detector. The PXRD pattern of Fe-ICR-5 was collected using a SmartLab diffractometer of Rigaku equipped with a Cu rotating anode, primary monochromator, capillary holder, and D/tex 250 detector.

The crystal structures of Fe-ICR-5 and Fe-ICR-7 were partially solved in the program Superflip[2] and consequently step-by-step completed by combination of the Rietveld refinement and manual fragment placement to the difference Fourier in the program MCE.[3] The procedure was identical for both crystal structures. In order to keep a reasonable geometry of the molecular model, bond length and bond angle restraints were introduced and one isotropic atomic displacement parameter (ADP) parameter was shared by C, O, and P atoms and one ADP was shared by Fe atoms. Hydrogen atoms were kept in their theoretical positions. At the final stage of the Rietveld refinement, the coordinates of C, O, P, and Fe atoms were refined using restraints discussed above together with their shared ADPs, unit cell

parameters, background, and scale factor. The results and the final profile fit are shown in Table S2 and Figures S15-S16.

The crystal structure of Al-ICR-4 was confirmed and refined by the Rietveld refinement in the Jana2006 software. The Fe-ICR-4 structure was taken as an initial crystal structure where all Fe atoms were replaced by Al atoms. At the final stage of the refinement, the rigid body approach was introduced for two phenyl rings (atoms C7-C12), where only position and rotation of the phenyl fragment was refined. The third phenyl ring occupies a special position and for that reason the atomic positions of C atoms in this phenyl ring were refined using bond and bond angle restraints as well as oxygen atoms connecting to phosphorus atoms. Hydrogen atoms were kept in their theoretical positions. Carbon and oxygen atoms shared one isotropic ADP, while phosphorus atoms had their own, and ADP of the aluminium atom was refined as harmonic. The final Rietveld refinement led to low agreement factors R_{wp} = 0.0298, R_p = 0.0349, *GOF* = 2.9 (Table S2). The final plot of the fit is in Figure S17.

Adsorption isotherms of N_2 were recorded using a Belsorp maxII instrument. Prior to adsorption experiments, the samples were evacuated at 80 °C for at least 24 h. Due to the microporous nature of Fe-ICR-2, Al-ICR-2, Fe-ICR-4, and Al-ICR-4, the determination of BET surface area did not provide reliable data (negative C value within the range P/P_0 = 0.05-0.3). Therefore, the surface areas of these ICRs were determined from the t-plot. The pore size distribution was calculated from the adsorption branch either using the NLDFT method for cylindrical pores (Fe-ICR-6, Al-ICR-6, Fe-ICR-7, Al-ICR-6) as provided by the Belsorp software or by the MP plot (Fe-ICR-2, Al-ICR-2, Fe-ICR-4, Al-ICR-4).

Thermal analyses (TG/DTA/MS) were carried out on a Setaram SETSYS Evolution-16-MS instrument coupled with a mass-spectrometer. The measurements were performed in synthetic air (flow rate 30 mL min^{-1}) from 30 to 750 °C with a heating rate of 5 °C min^{-1}. Fourier transform infrared spectra (FTIR) were collected on a Nicolet NEXUS 670-FT spectrometer in KBr pellets (2000−400 cm^{-1}).

An HPLC-DAD DIONEX UltiMate 3000 instrument was used for the concentration analysis of BPA in sorption experiments. The HPLC system was equipped with a diode array detector, 20 µL sampling loop, and Kinetex 2.6 µm C18 column (Phenomenex, USA, 50 mm x 3 mm). Methanol/water mixture was used as a mobile phase (0.5 mL min^{-1}, both solvents contained 0.1 % HCOOH) under isocratic elution ratio of 55/45 (v/v). The time of analysis was set to 3

min. The signals were collected at 215 nm. The concentrations of BPA were determined using the standard calibration curve method.

Table S1. Elemental analysis of ICR MOFs.

Sample	Formula[a]	C: W_{calcd}	C: W_{found}	H: W_{calcd}	H: W_{found}
Fe-ICR-2	$Fe_2(C_8H_{10}O_4P_2)_3$	35.67	35.74	3.74	3.73
Fe-ICR-4	$Fe_2(C_{18}H_{14}O_4P_2)_3$	54.94	52.97	3.59	3.62
Fe-ICR-6	$Fe_2(C_{14}H_{14}O_4P_2)_3$	48.68	48.57	4.08	4.18
Fe-ICR-7	$Fe_2(C_{24}H_{18}O_4P_2)_3$	61.38	60.94	3.86	3.74
Al-ICR-2	$Al_2(C_8H_{10}O_4P_2)_3$	38.42	37.59	4.03	4.09
Al-ICR-4	$Al_2(C_{18}H_{14}O_4P_2)_3$	57.77	55.15	3.77	3.80
Al-ICR-6	$Al_2(C_{14}H_{14}O_4P_2)_3$	51.55	49.43	4.33	4.33
Al-ICR-7	$Al_2(C_{24}H_{18}O_4P_2)_3$	64.01	62.62	4.03	4.05

[a] The formulas are based on $M_2(linker)_3$ ratio.

FTIR spectrum of Fe-ICR-2 is presented in the previous publication.[4]

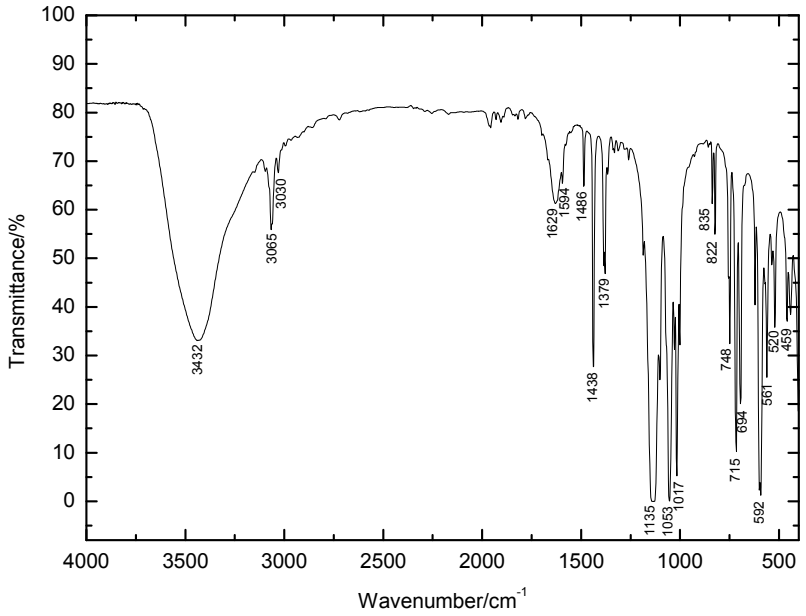

Figure S1. FTIR spectrum of Fe-ICR-4.

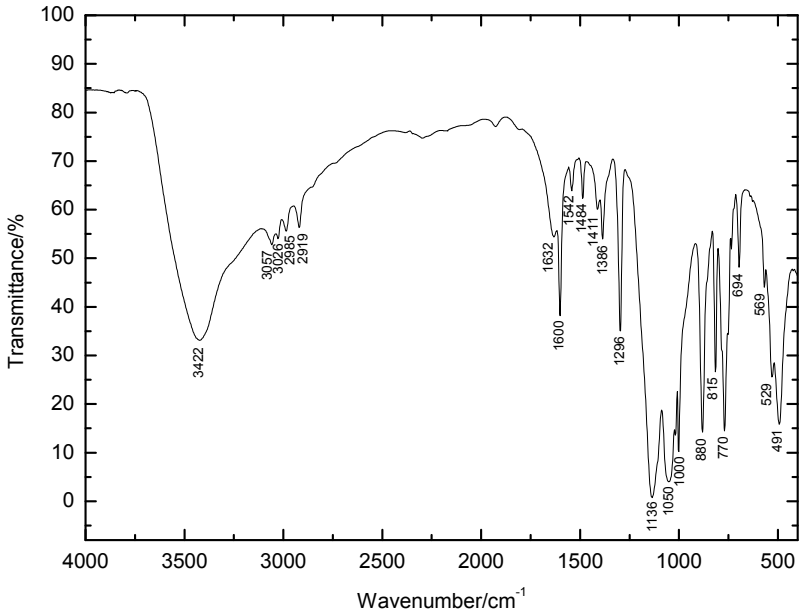

Figure S2. FTIR spectrum of Fe-ICR-6.

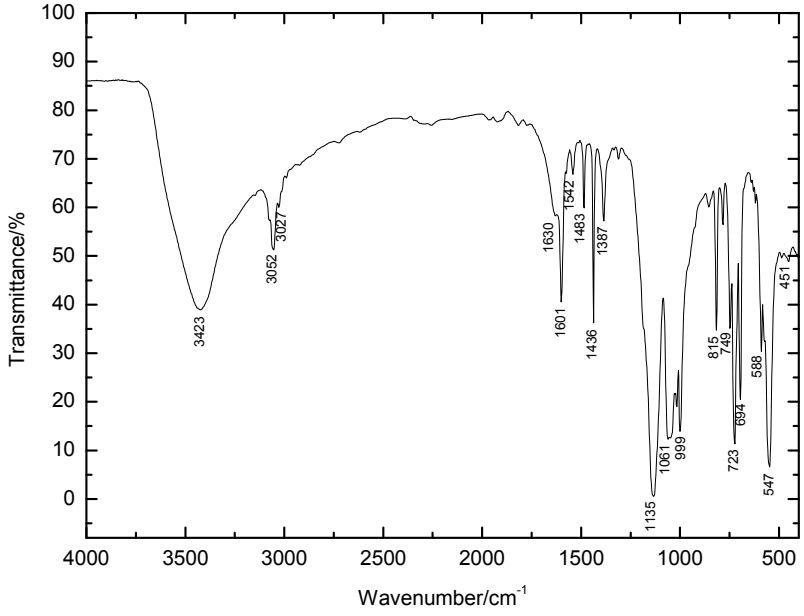

Figure S3. FTIR spectrum of Fe-ICR-7.

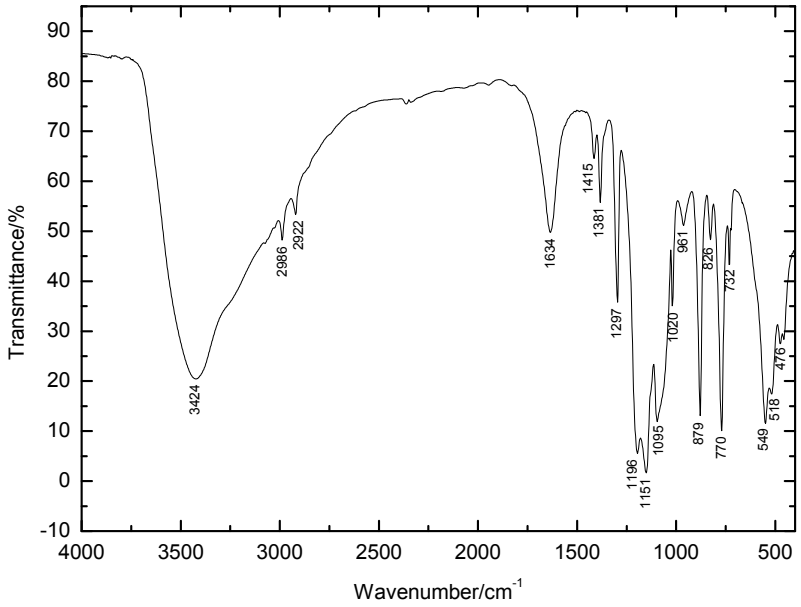

Figure S4. FTIR spectrum of Al-ICR-2.

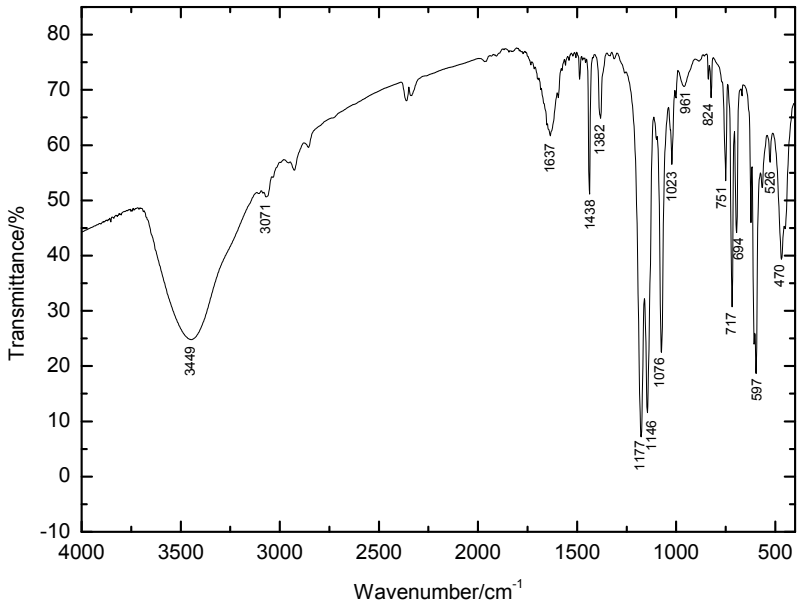

Figure S5. FTIR spectrum of Al-ICR-4.

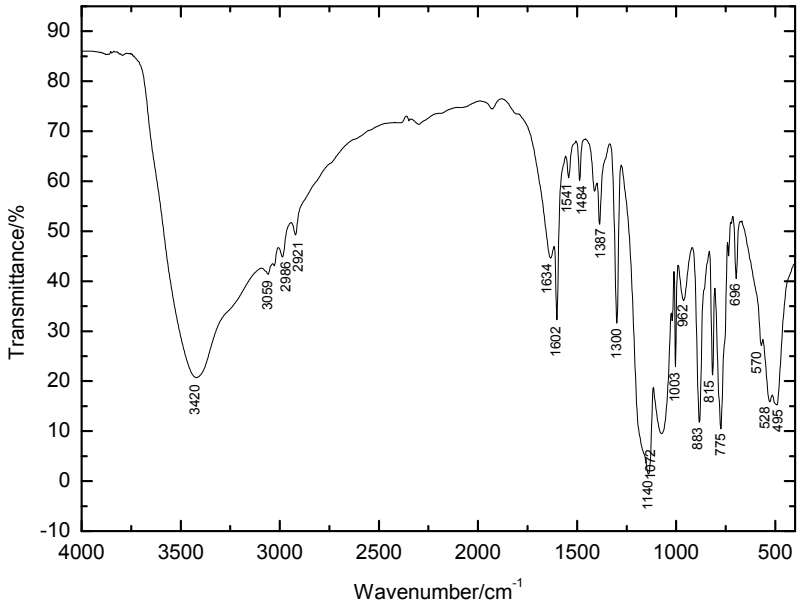

Figure S6. FTIR spectrum of Al-ICR-6.

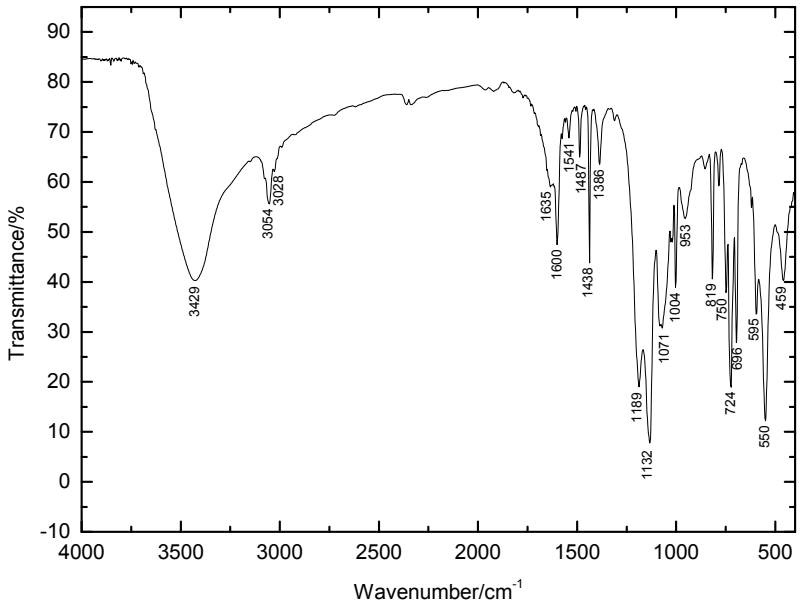

Figure S7. FTIR spectrum of Al-ICR-7.

TGA/DTA curves and the evolution of gases for Fe-ICR-2 in air are published in the previous publication.[4]

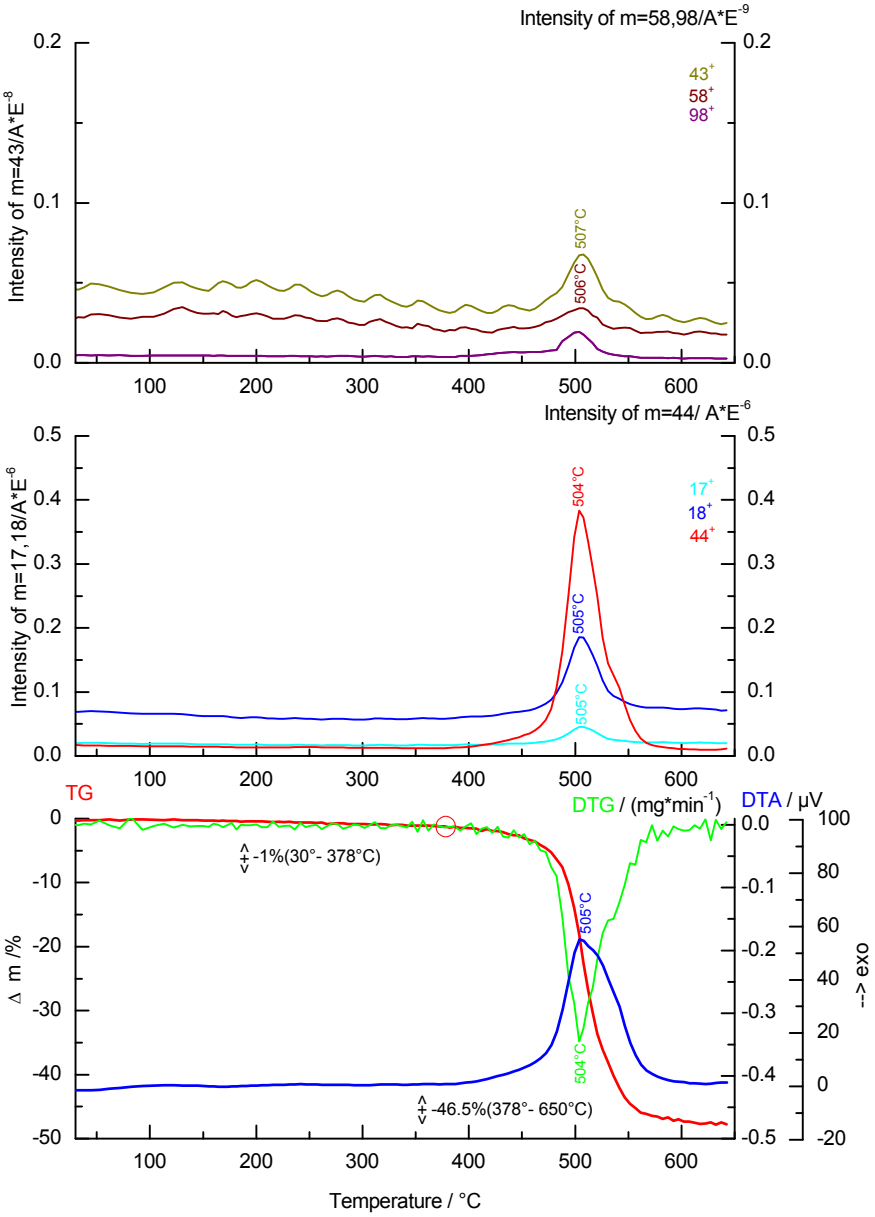

Figure S8. TGA/DTA curves and the evolution of gases for Fe-ICR-4 in air; m/z = 17 – OH, m/z = 18 –H_2O, m/z = 44 – CO_2, m/z = 43 and 58 – acetone, and m/z = 98 – H_3PO_4.

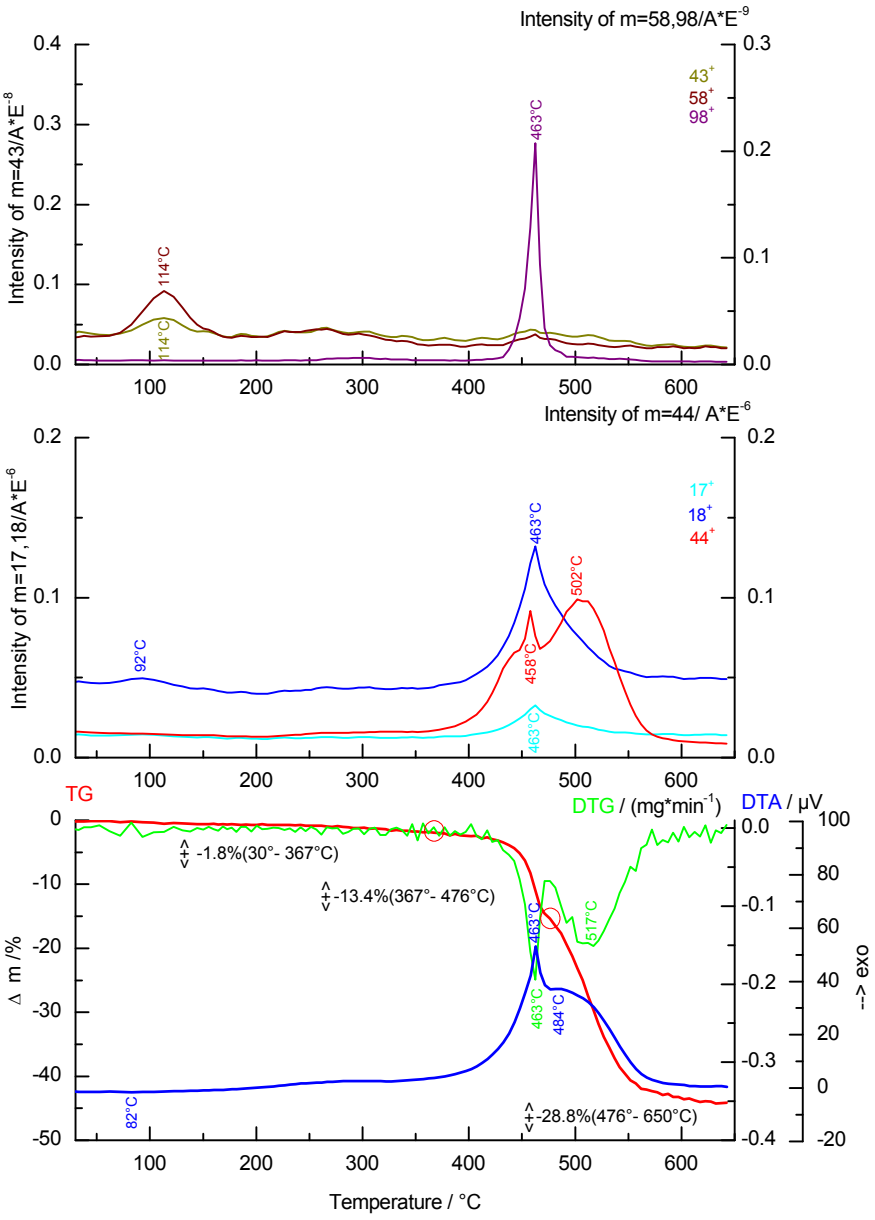

Figure S9. TGA/DTA curves and the evolution of gases for Fe-ICR-6 in air; m/z = 17 – OH, m/z = 18 –H_2O, m/z = 44 – CO_2, m/z = 43 and 58 – acetone, and m/z = 98 – H_3PO_4.

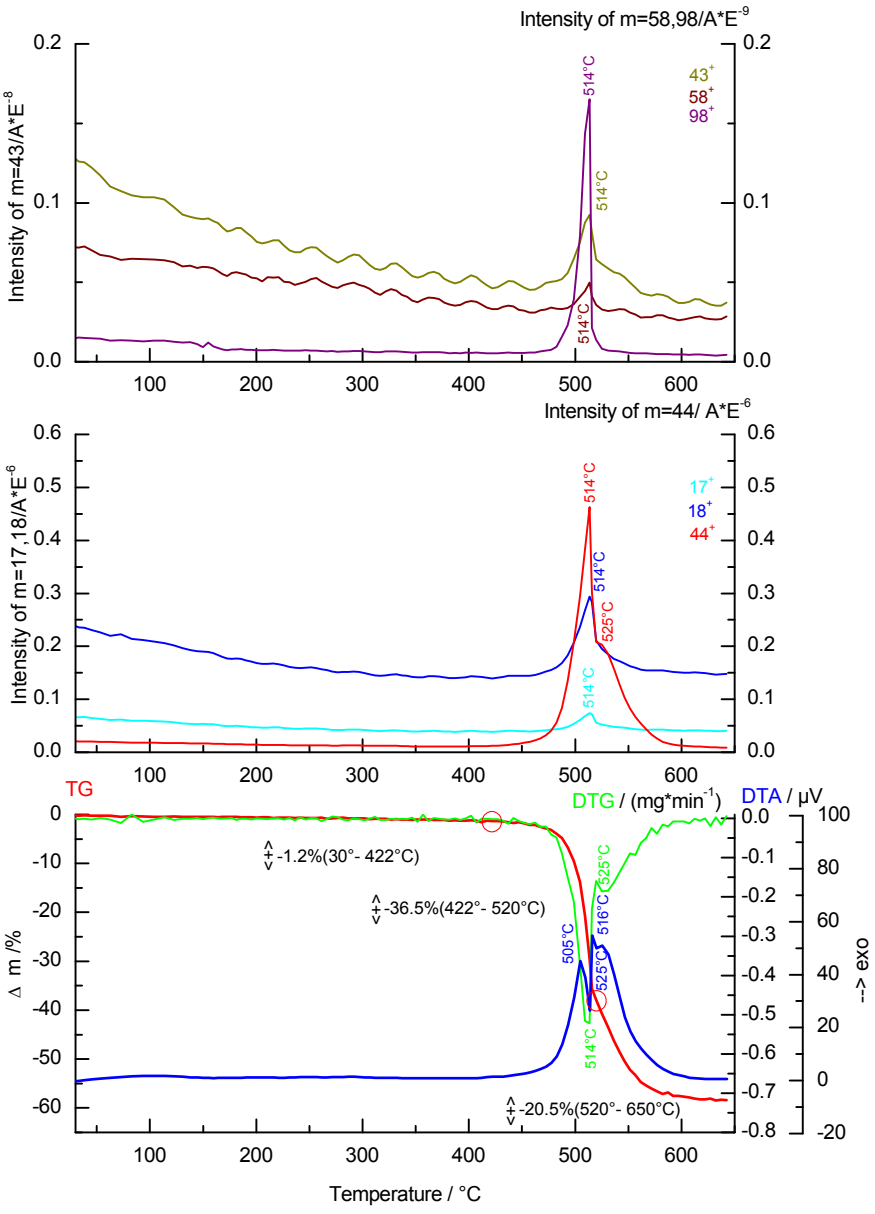

Figure S10. TGA/DTA curves and the evolution of gases for Fe-ICR-7 in air; m/z = 17 – OH, m/z = 18 –H_2O, m/z = 44 – CO_2, m/z = 43 and 58 – acetone, and m/z = 98 – H_3PO_4.

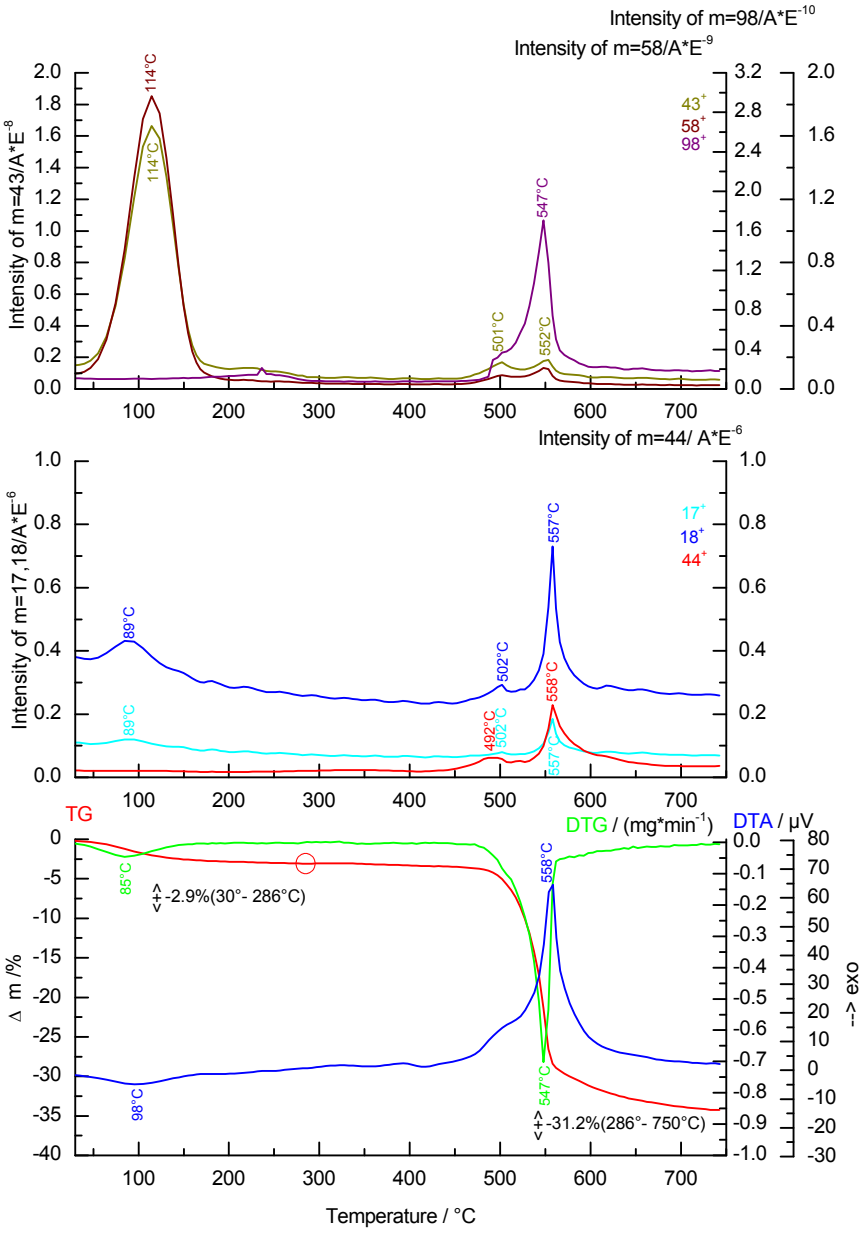

Figure S11. TGA/DTA curves and the evolution of gases for Al-ICR-2 in air; m/z = 17 – OH, m/z = 18 –H_2O, m/z = 44 – CO_2, m/z = 43 and 58 – acetone, and m/z = 98 – H_3PO_4.

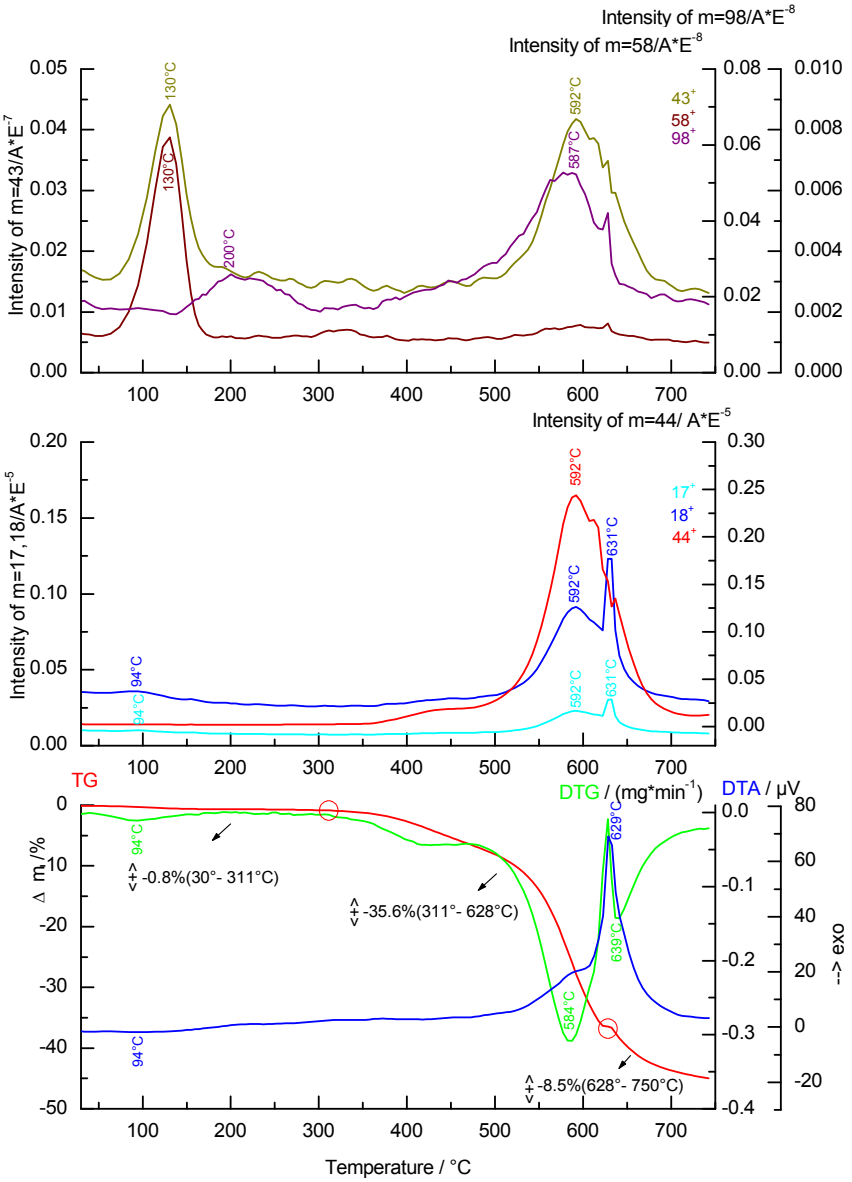

Figure S12. TGA/DTA curves and the evolution of gases for Al-ICR-4 in air; m/z = 17 – OH, m/z = 18 –H_2O, m/z = 44 – CO_2, m/z = 43 and 58 – acetone, and m/z = 98 – H_3PO_4.

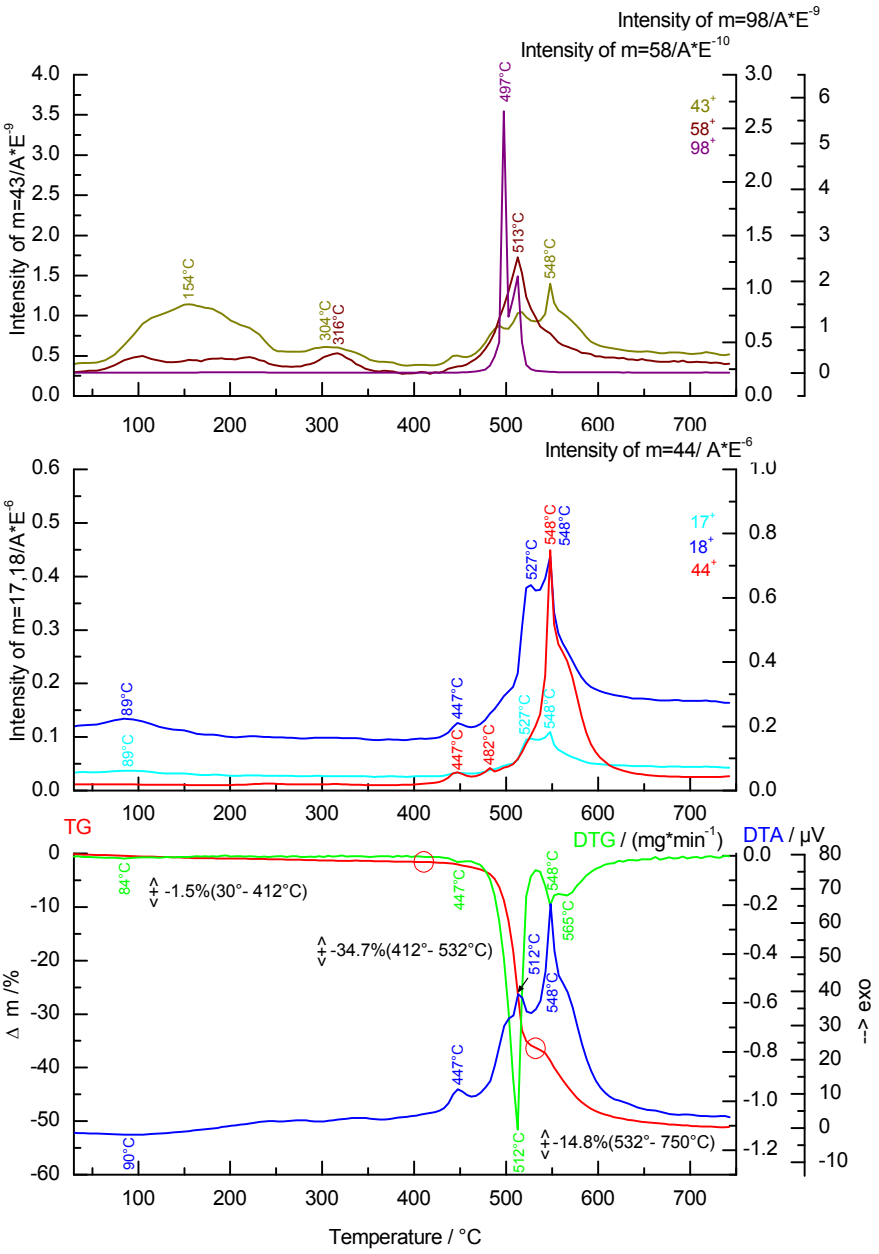

Figure S13. TGA/DTA curves and the evolution of gases for Al-ICR-6 in air; m/z = 17 – OH, m/z = 18 –H_2O, m/z = 44 – CO_2, m/z = 43 and 58 – acetone, and m/z = 98 – H_3PO_4.

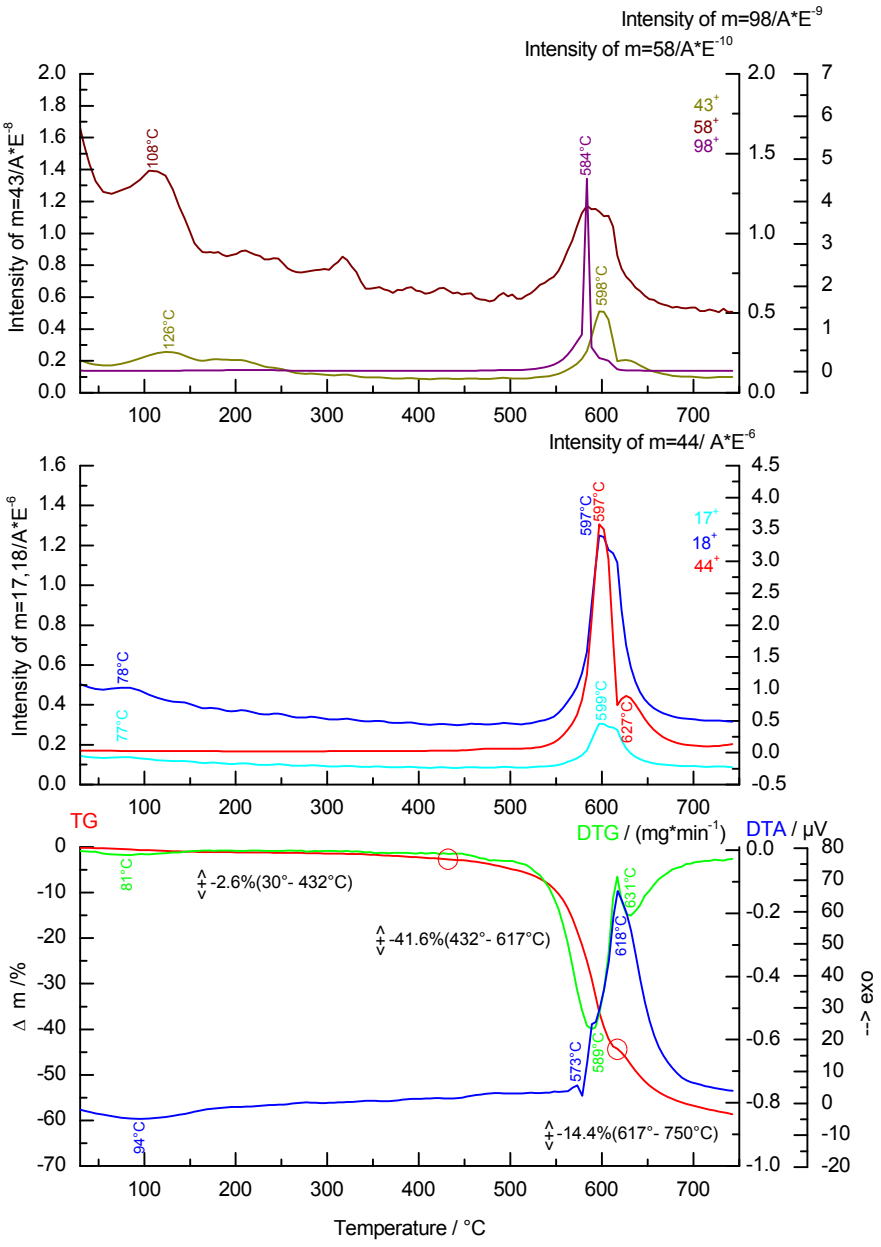

Figure S14. TGA/DTA curves and the evolution of gases for Al-ICR-7 in air; m/z = 17 – OH, m/z = 18 –H_2O, m/z = 44 – CO_2, m/z = 43 and 58 – acetone, and m/z = 98 – H_3PO_4.

Table S2. Crystallographic data.

	Fe-ICR-5	Fe-ICR-7	Al-ICR-4
Formula	$Fe\ P_2\ O_4\ C_{14}\ H_8$	$Fe_2\ P_6\ O_{12}\ C_{72}\ H_{54}$	$Al\ P_3\ O_6\ C_{27}\ H_{21}$
a	20.9684(8)	25.0259(11)	17.20746(15)
b	5.0946(2)	25.0259(11)	17.20746(15)
c	13.9685(6)	9.5800(8)	9.39191(14)
β	108.6347(14)	-	-
Volume	1413.97(10)	5196.1(5)	2408.34(5)
Crystal system	monoclinic	trigonal	trigonal
Space group	$P2_1/a$	*P*-3	*P*-3
R_p	2.06	5.64	3.37
R_{wp}	3.40	7.56	2.79
GOF	4.69	6.46	2.73

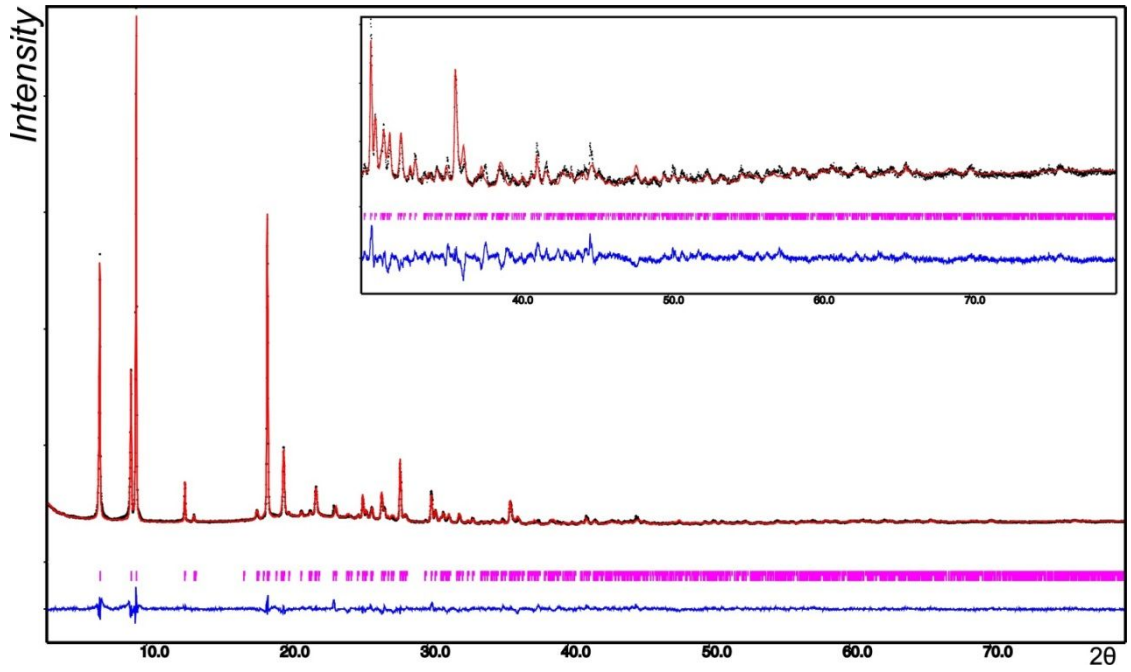

Figure S15. Final Rietveld fit of Fe-ICR-5. Black dots – measured data, red line – calculated profile, blue line – difference curve.

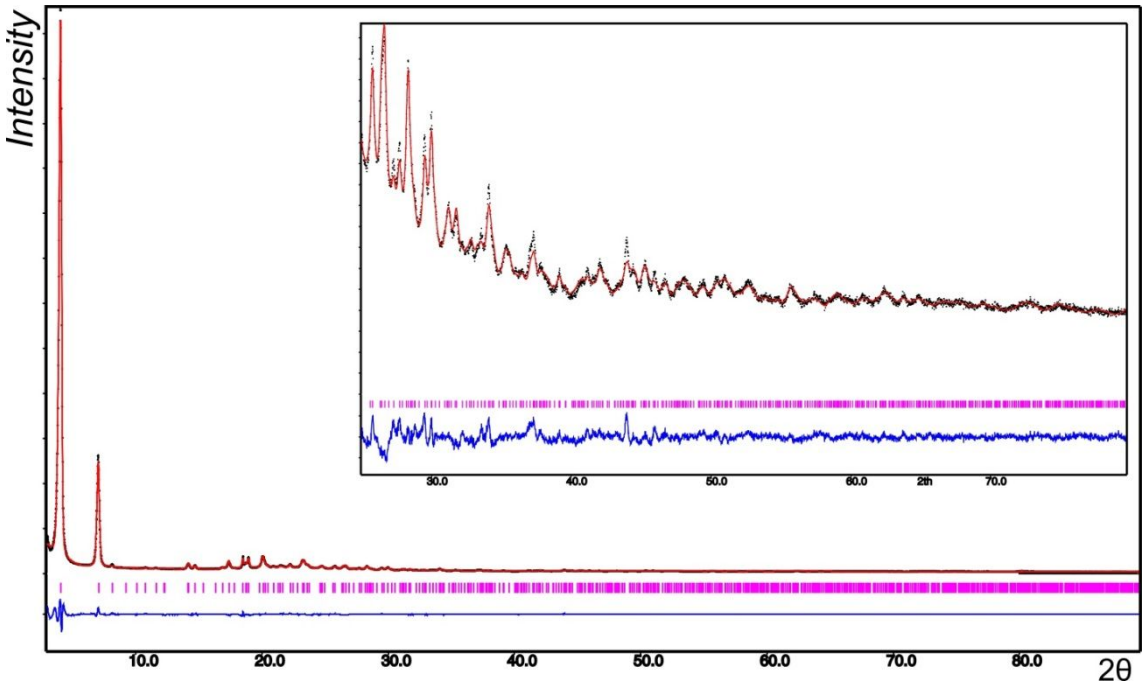

Figure S16. Final Rietveld fit of Fe-ICR-7. Black dots – measured data, red line – calculated profile, blue line – difference curve.

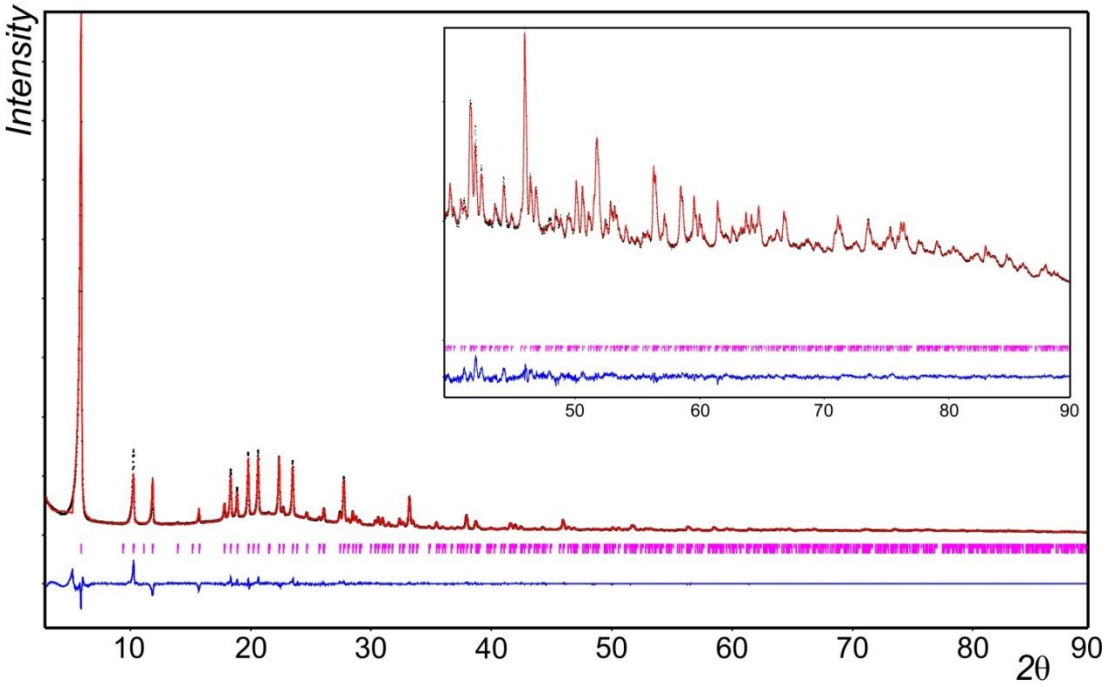

Figure S17. Final Rietveld fit of Al-ICR-4. Black dots – measured data, red line – calculated profile, blue line – difference curve.

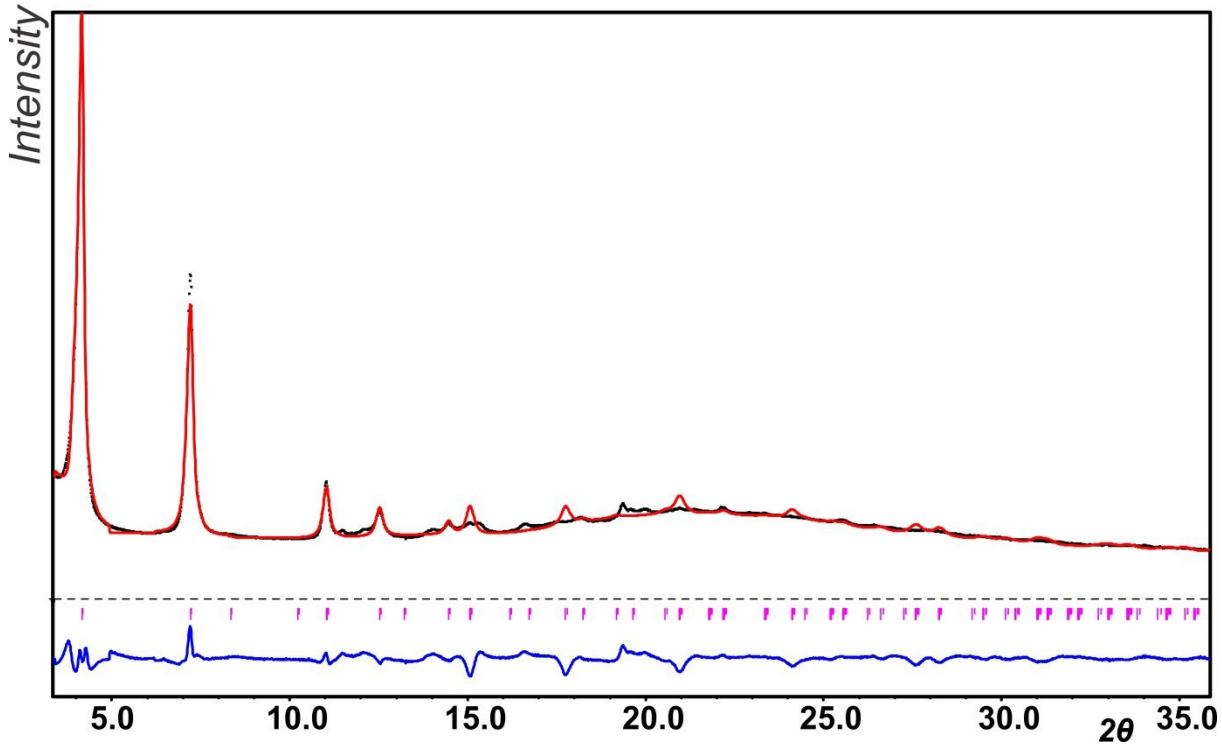

Figure S18. Final Rietveld fit of Fe-ICR-6. Black dots – measured data, red line – calculated profile, blue line – difference curve.

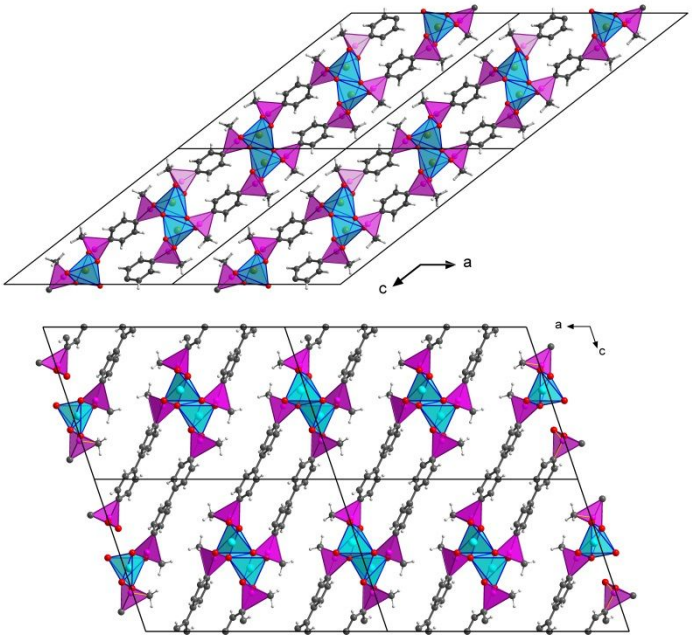

Figure S19. Comparison of the crystal structures of Fe-ICR-3 (top)[4] and Fe-ICR-5 (bottom, this paper).

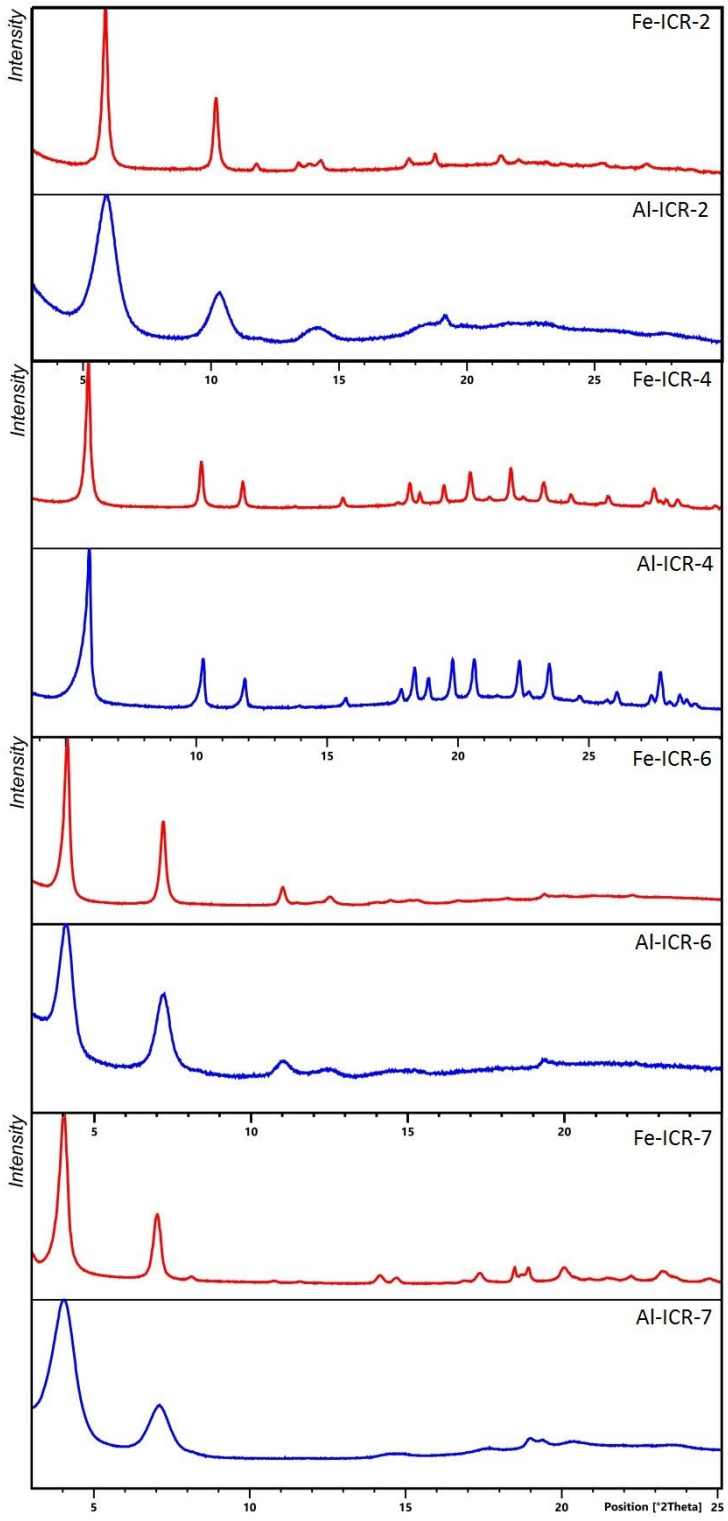

Figure S20. Comparison of PXRD patterns of Al-ICR and Fe-ICR MOFs.

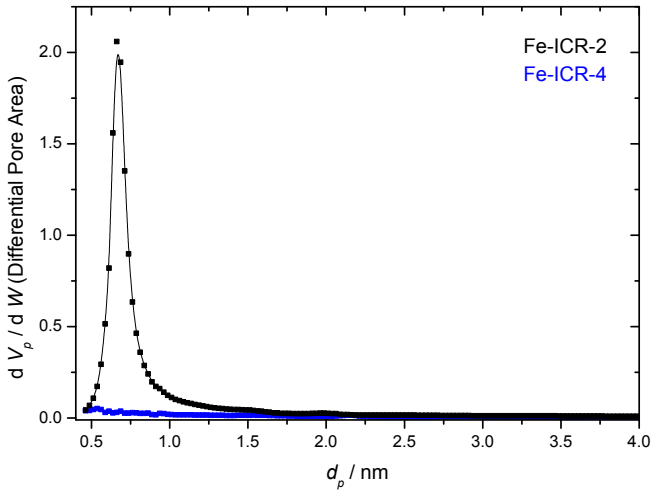

Figure S21. Pore size distribution of Fe-ICR-2 and Fe-ICR-4 calculated by the MP plot.

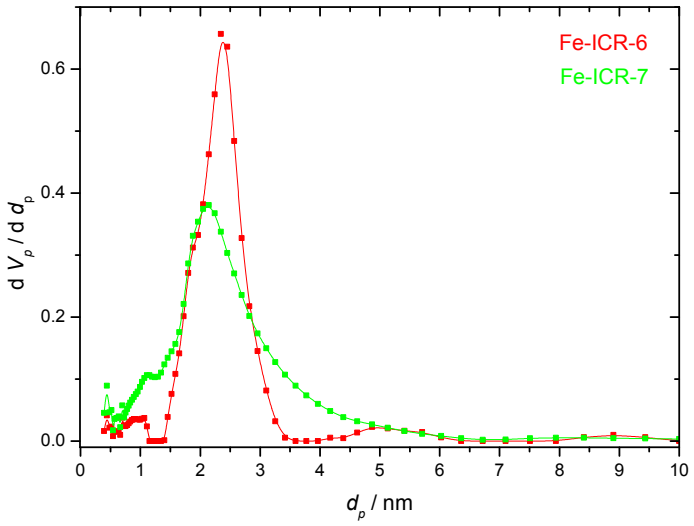

Figure S22. Pore size distribution of Fe-ICR-6 and Fe-ICR-7 calculated using the NLDFT method for cylindrical pores.

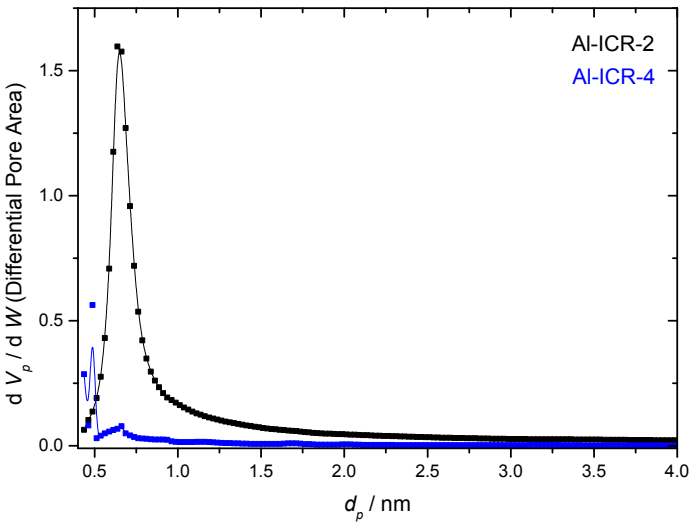

Figure S23. Pore size distribution of Al-ICR-2 and Al-ICR-4 calculated by the MP plot.

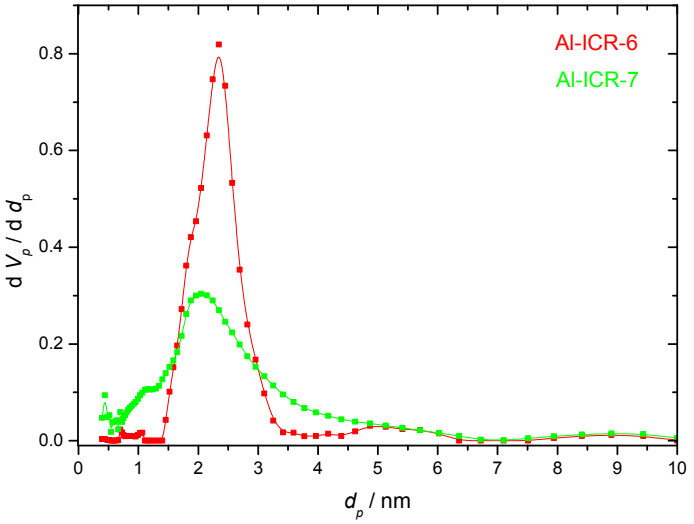

Figure S24. Pore size distribution of Al-ICR-6 and Al-ICR-7 calculated using the NLDFT method for cylindrical pores.

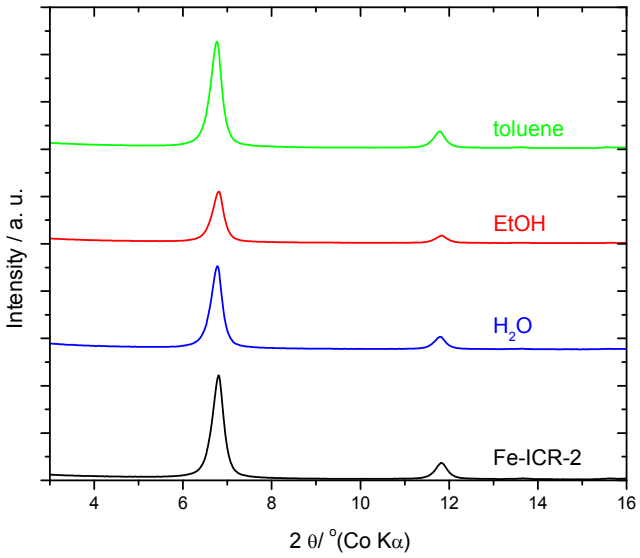

Figure S25. PXRD patterns of as-synthetized Fe-ICR-2 (bottom) and Fe-ICR-2 after 24 h treatment in H_2O, EtOH, and toluene at room temperature. The diffractograms are vertically shifted to avoid overlaps.

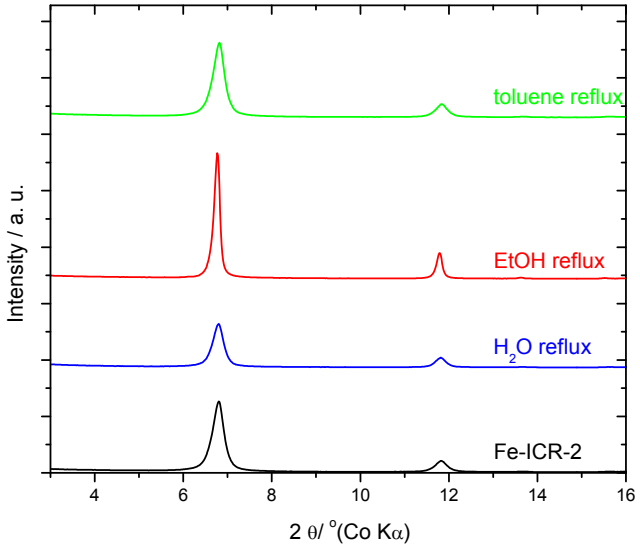

Figure S26. PXRD patterns of as-synthetized Fe-ICR-2 (bottom) and Fe-ICR-2 after 24 h treatment in boiling H_2O, EtOH, and toluene. The diffractograms are vertically shifted to avoid overlaps.

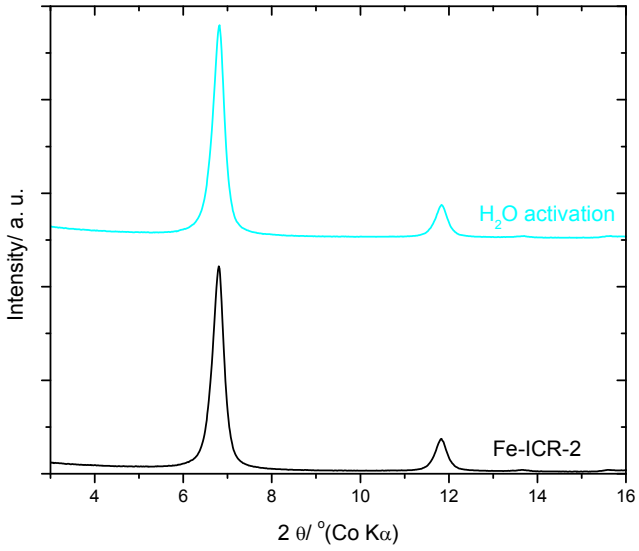

Figure S27. PXRD patterns of as-synthetized Fe-ICR-2 (bottom) and Fe-ICR-2 activated from water. The diffractograms are vertically shifted to avoid overlaps.

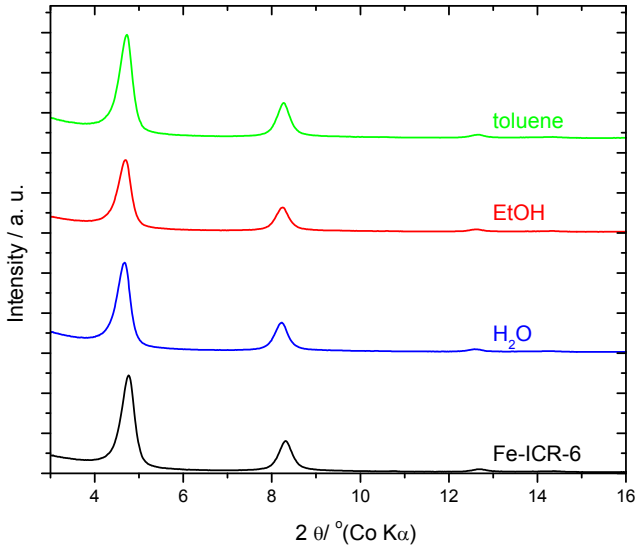

Figure S28. PXRD patterns of as-synthetized Fe-ICR-6 (bottom) and Fe-ICR-6 after 24 h treatment in H_2O, EtOH, and toluene at room temperature. The diffractograms are vertically shifted to avoid overlaps.

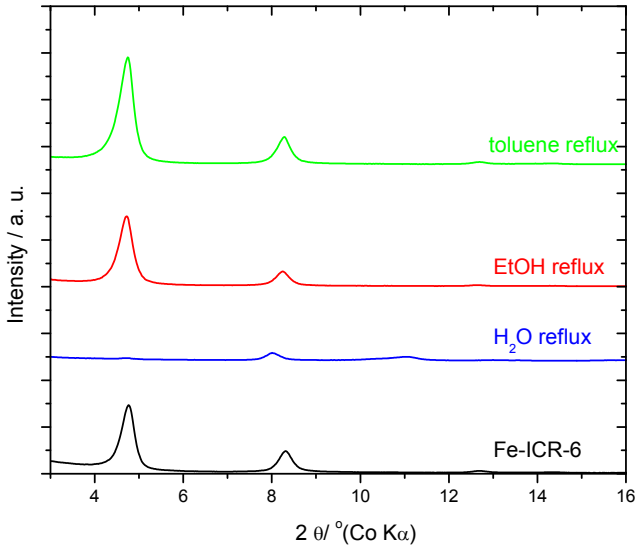

Figure S29. PXRD patterns of as-synthetized Fe-ICR-6 (bottom) and Fe-ICR-6 after 24 h in boiling H_2O, EtOH, and toluene. The diffractograms are vertically shifted to avoid overlaps.

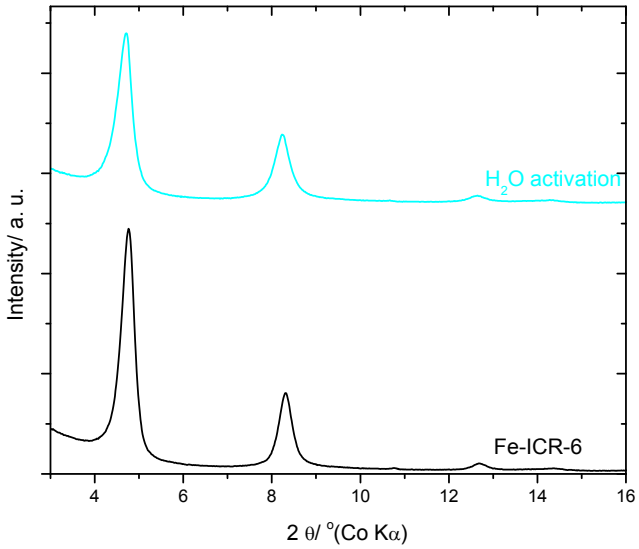

Figure S30. PXRD patterns of as-synthetized Fe-ICR-6 (bottom) and Fe-ICR-6 activated from water. The diffractograms are vertically shifted to avoid overlaps.

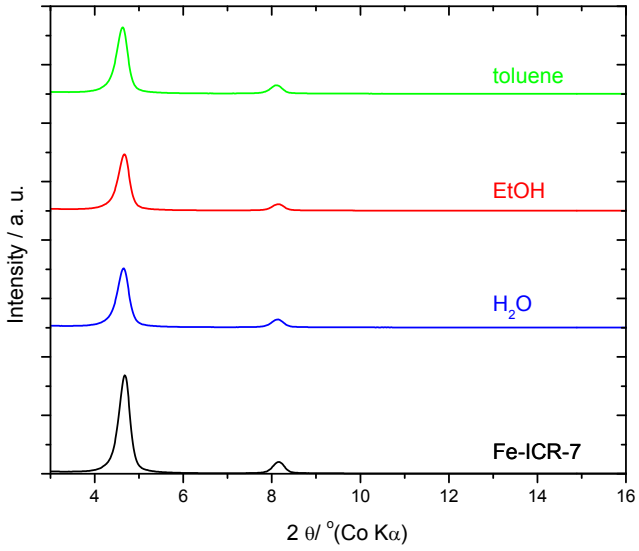

Figure S31. PXRD patterns of as-synthetized Fe-ICR-7 (bottom) and Fe-ICR-7 after 24 h treatment in H_2O, EtOH, and toluene at room temperature. The diffractograms are vertically shifted to avoid overlaps.

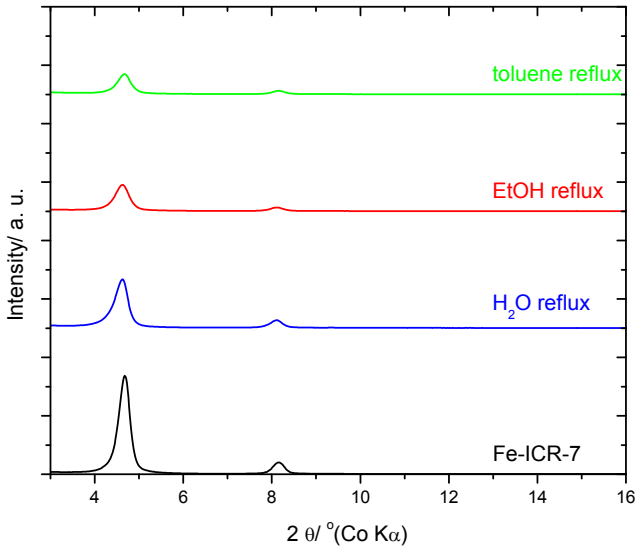

Figure S32. PXRD patterns of as-synthetized Fe-ICR-7 and Fe-ICR-7 after 24 h treatment in boiling H_2O, EtOH, and toluene. The diffractograms are vertically shifted to avoid overlaps.

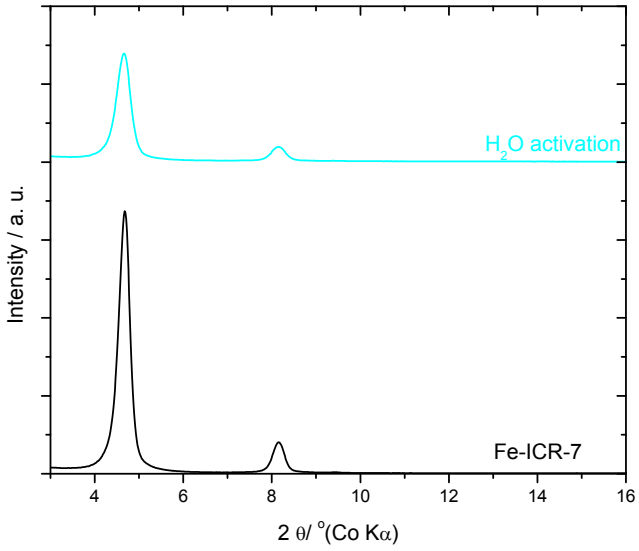

Figure S33. PXRD patterns of as-synthetized Fe-ICR-7 (bottom) and Fe-ICR-7 activated from water. The diffractograms are vertically shifted to avoid overlaps.

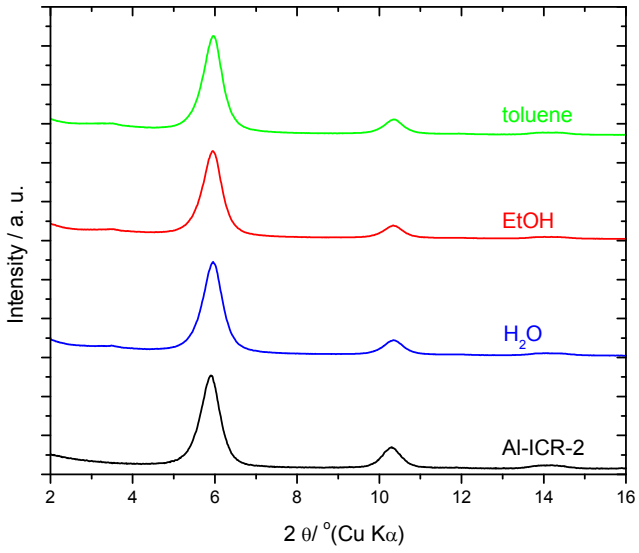

Figure S34. PXRD patterns of as-synthetized Al-ICR-2 and Al-ICR-2 after 24 h treatment in H_2O, EtOH, and toluene at room temperature. The diffractograms are vertically shifted to avoid overlaps.

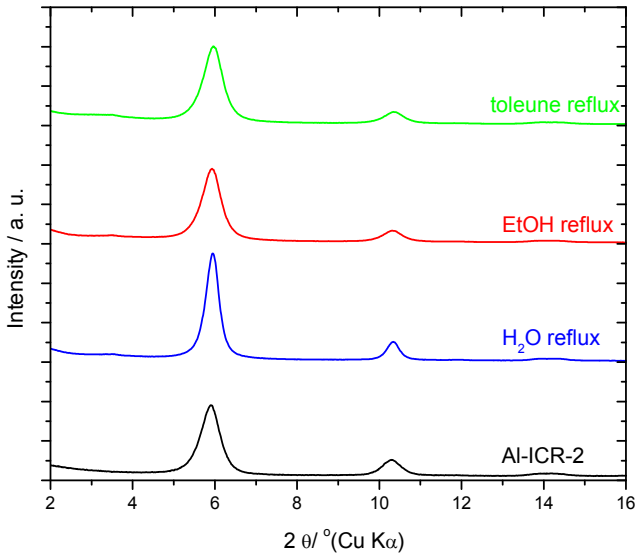

Figure S35. PXRD patterns of as-synthetized Al-ICR-2 (bottom) and Al-ICR-2 after 24 h treatment in boiling H_2O, EtOH, and toluene. The diffractograms are vertically shifted to avoid overlaps.

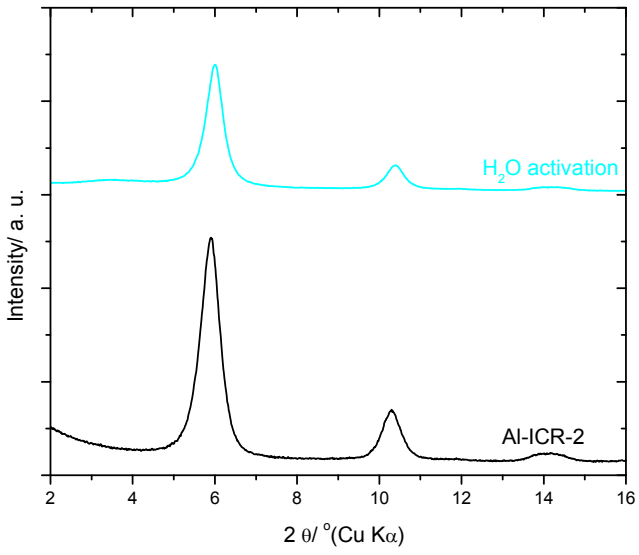

Figure S36. PXRD patterns of as-synthetized Al-ICR-2 (bottom) and Al-ICR-2 activated from water. The diffractograms are vertically shifted to avoid overlaps.

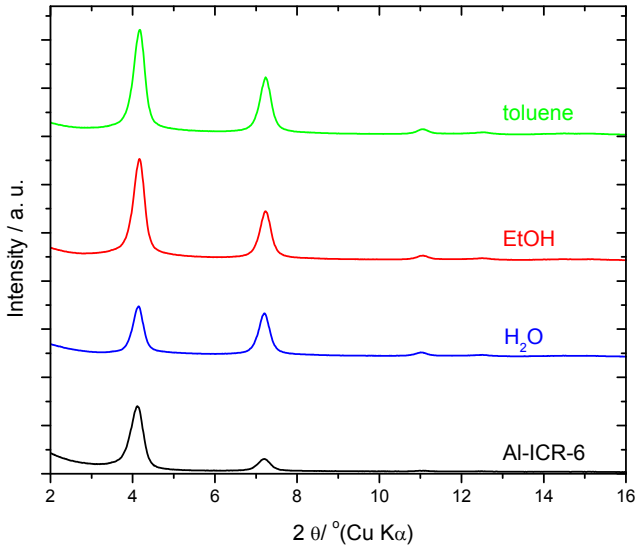

Figure S37. PXRD patterns of as-synthetized Al-ICR-6 (bottom) and Al-ICR-6 after 24 h treatment in H_2O, EtOH, and toluene at RT. The diffractograms are vertically shifted to avoid overlaps.

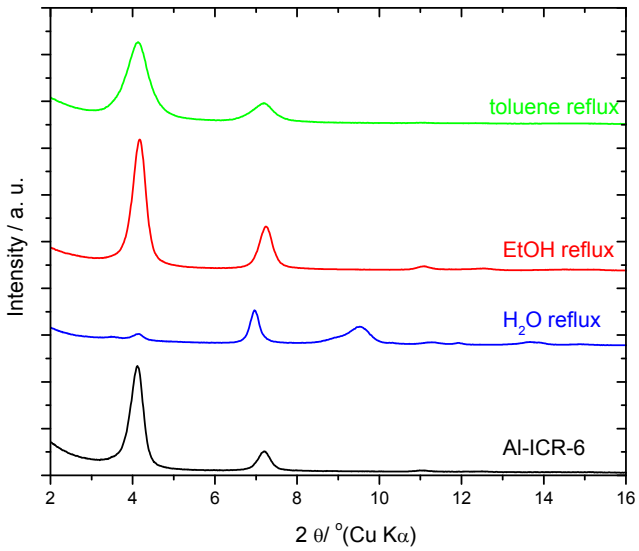

Figure S38. PXRD patterns of as-synthetized Al-ICR-6 (bottom) and Al-ICR-6 after 24 h treatment in boiling H_2O, EtOH, and toluene. The diffractograms are vertically shifted to avoid overlaps.

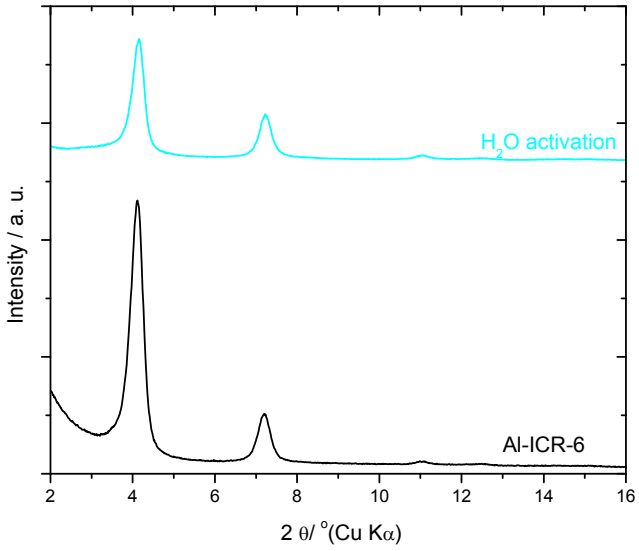

Figure S39. PXRD patterns of as-synthetized Al-ICR-6 (bottom) and Al-ICR-6 activated from water. The diffractograms are vertically shifted to avoid overlaps.

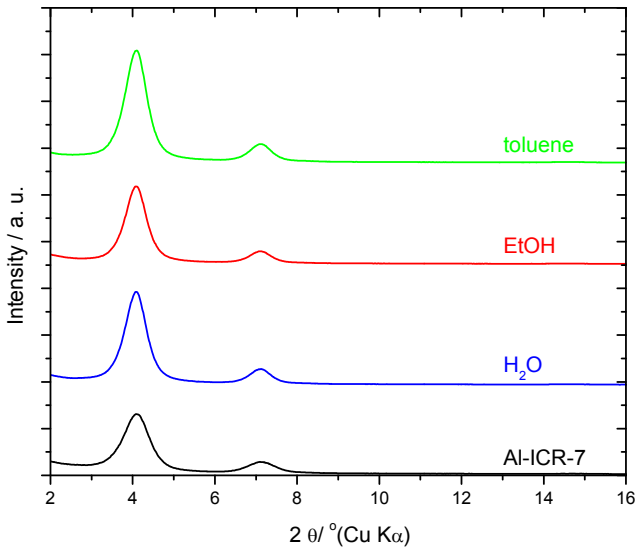

Figure S40. PXRD patterns of as-synthetized Al-ICR-7 (bottom) and Al-ICR-7 after 24 h treatment in H_2O, EtOH, and toluene at RT. The diffractograms are vertically shifted to avoid overlaps.

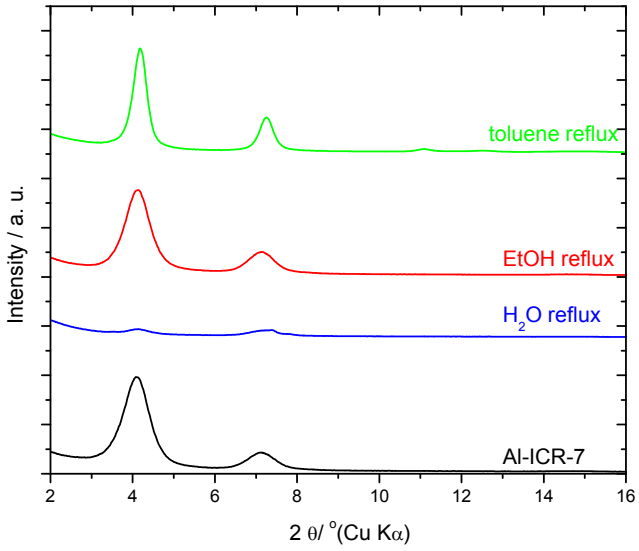

Figure S41. PXRD patterns of as-synthetized Al-ICR-7 (bottom) nad Al-ICR-7 after 24 h treatment in boiling H_2O, EtOH, and toluene. The diffractograms are vertically shifted to avoid overlaps.

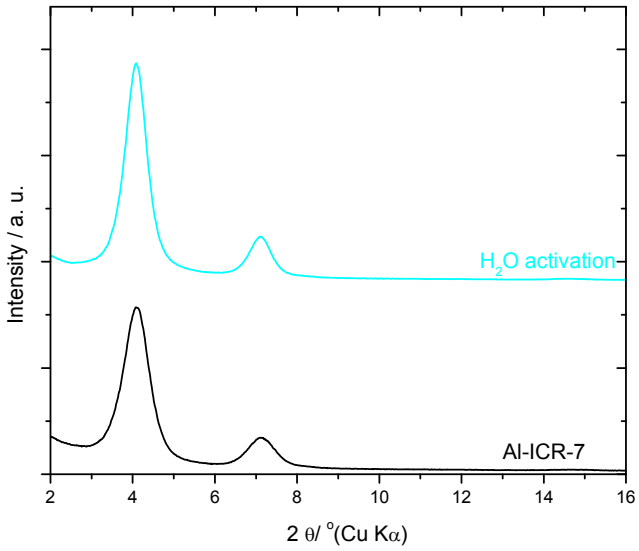

Figure S42. PXRD patterns of as-synthetized Al-ICR-7 (bottom) and Al-ICR-7 activated from water. The diffractograms are vertically shifted to avoid overlaps.

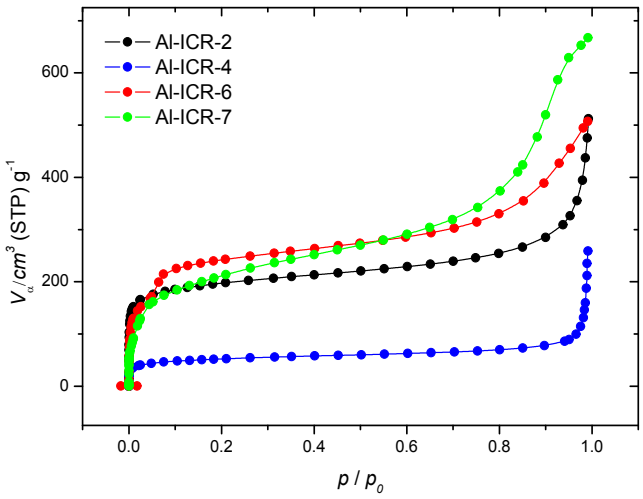

Figure S43. Nitrogen adsorption isotherms of as-synthetized Al-ICR-2, Al-ICR-4, Al-ICR-6, and Al-ICR-7.

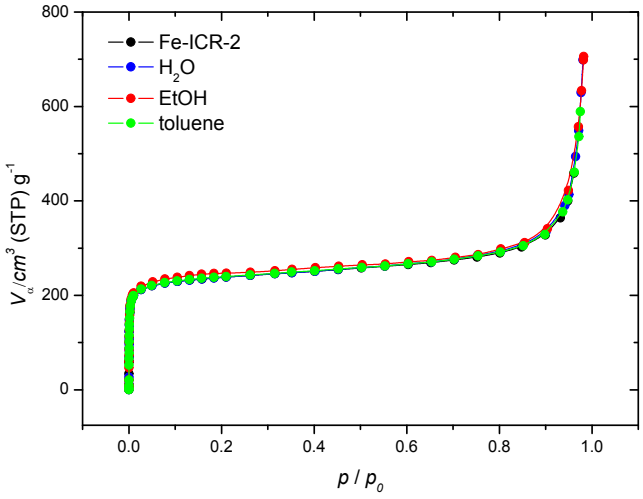

Figure S44. Nitrogen adsorption isotherms of as-synthetized Fe-ICR-2 (black) and Fe-ICR-2 after 24 h treatment in H_2O, EtOH, and toluene at RT.

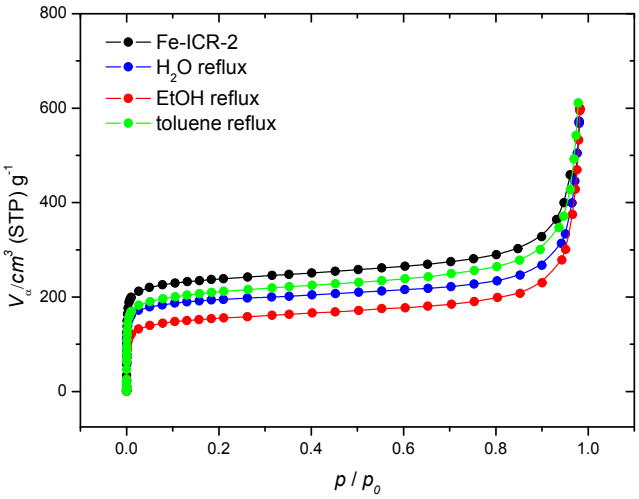

Figure S45. Nitrogen adsorption isotherms of as-synthetized Fe-ICR-2 (black) and Fe-ICR-2 after 24 h treatment in boiling H_2O, EtOH, and toluene.

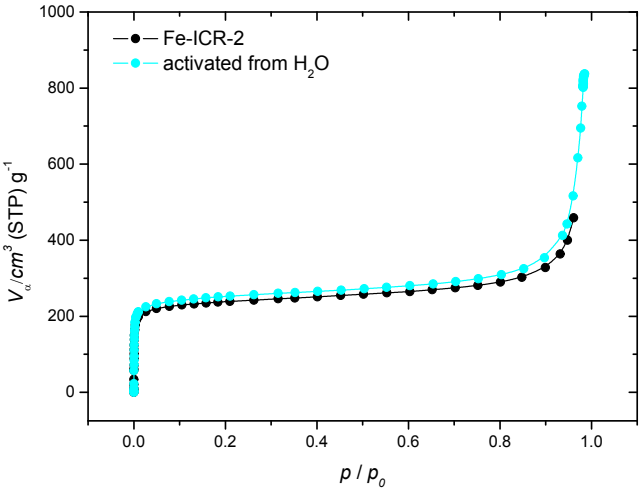

Figure S46. Nitrogen adsorption isotherms of as-synthetized Fe-ICR-2 (black) and Fe-ICR-2 activated from water.

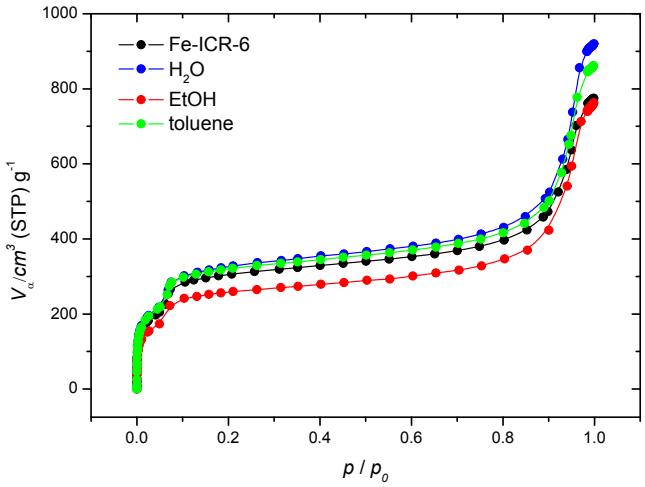

Figure S47. Nitrogen adsorption isotherms of as-synthetized Fe-ICR-6 (black) and Fe-ICR-6 after 24 h treatment in H_2O, EtOH, and toluene at RT.

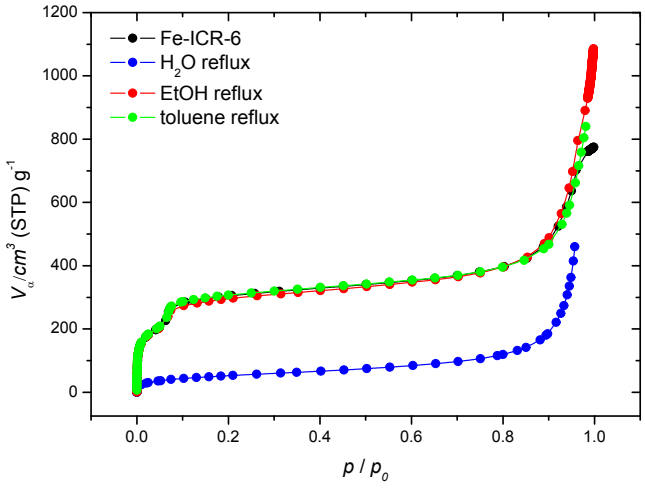

Figure S48. Nitrogen adsorption isotherms of as-synthetized Fe-ICR-6 (black) and Fe-ICR-6 after 24 h treatment in boiling H_2O, EtOH, and toluene.

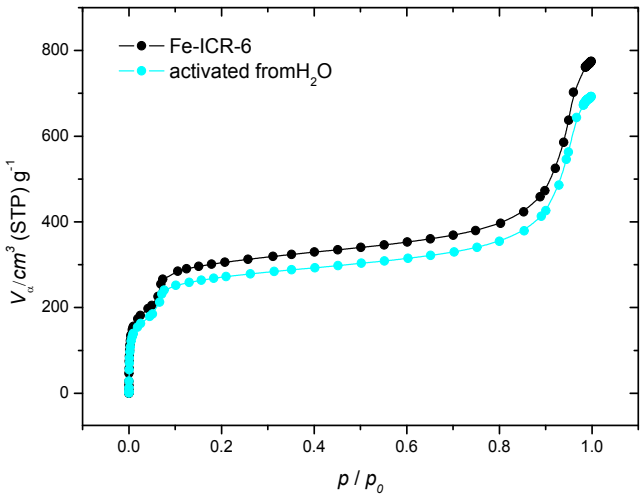

Figure S49. Nitrogen adsorption isotherms of as-synthetized Fe-ICR-6 (black) and Fe-ICR-6 activated from water.

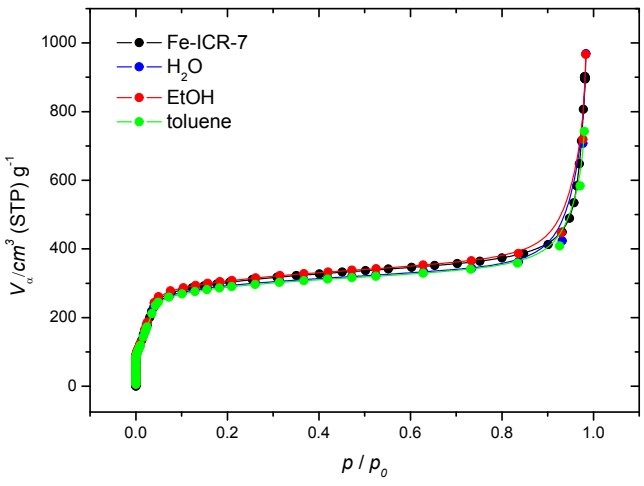

Figure S50. Nitrogen adsorption isotherms of as-synthetized Fe-ICR-7 (black) and Fe-ICR-7 after 24 h treatment in H_2O, EtOH, and toluene at RT.

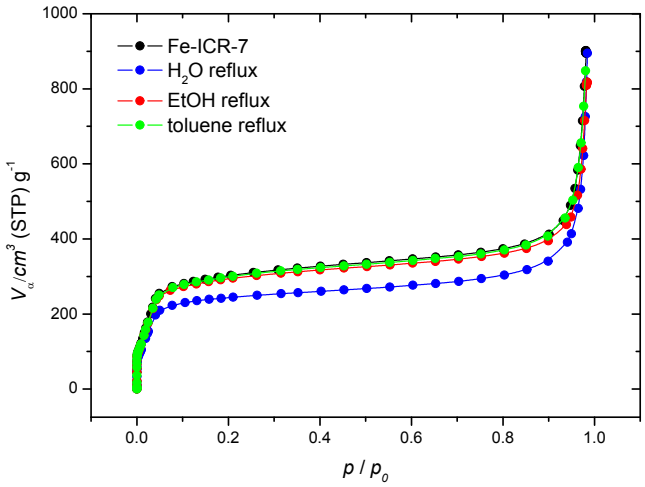

Figure S51. Nitrogen adsorption isotherms of as-synthetized Fe-ICR-7 (black) and Fe-ICR-7 after 24 h treatment in boiling H_2O, EtOH, and toluene.

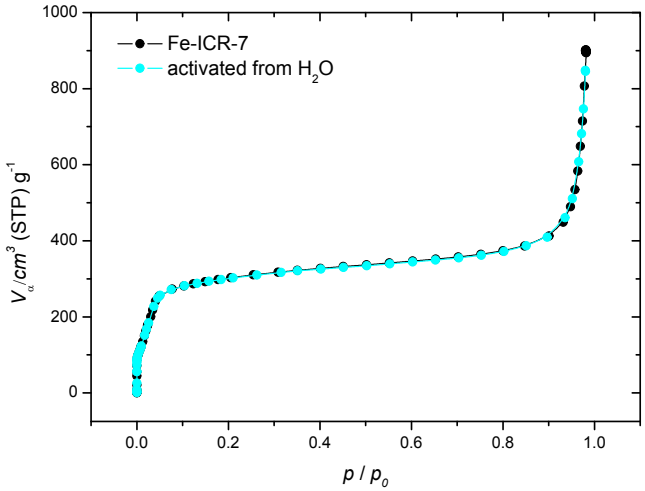

Figure S52. Nitrogen adsorption isotherms of as-synthetized Fe-ICR-7 (black) and Fe-ICR-7 activated from water.

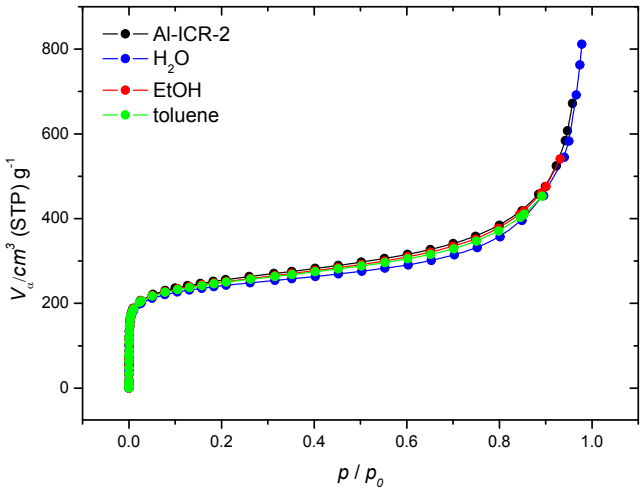

Figure S53. Nitrogen adsorption isotherms of as synthetized Al-ICR-2 (black) and Al-ICR-2 after 24 h treatment in H_2O, EtOH, and toluene at RT.

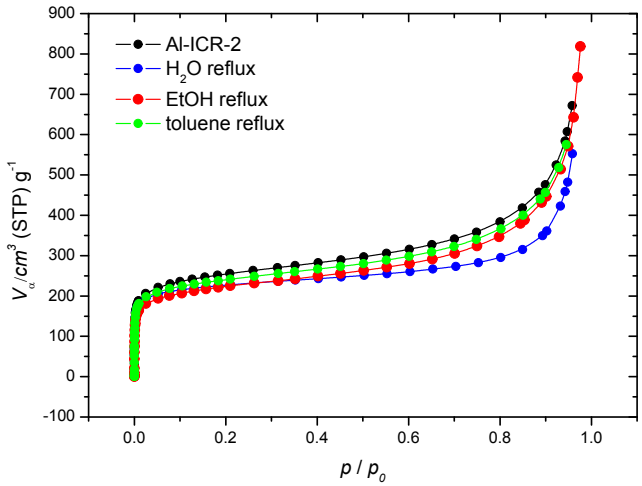

Figure S54. Nitrogen adsorption isotherms of as-synthetized Al-ICR-2 (black) and Al-ICR-2 after 24 h treatment in boiling H_2O, EtOH, and toluene.

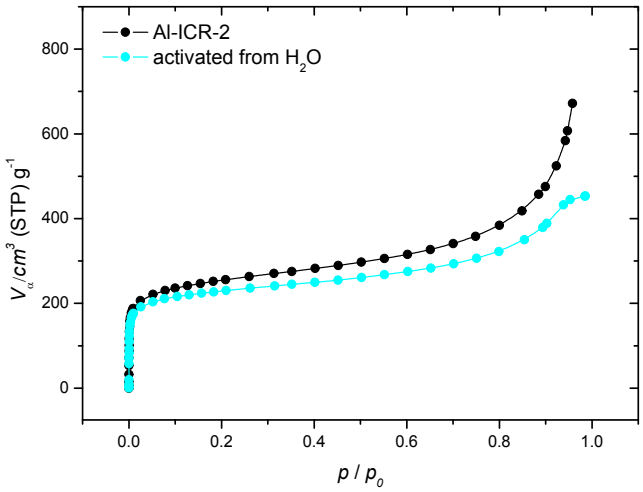

Figure S55. Nitrogen adsorption isotherms of as-synthetized Al-ICR-2 (black) and Al-ICR-2 activated from water.

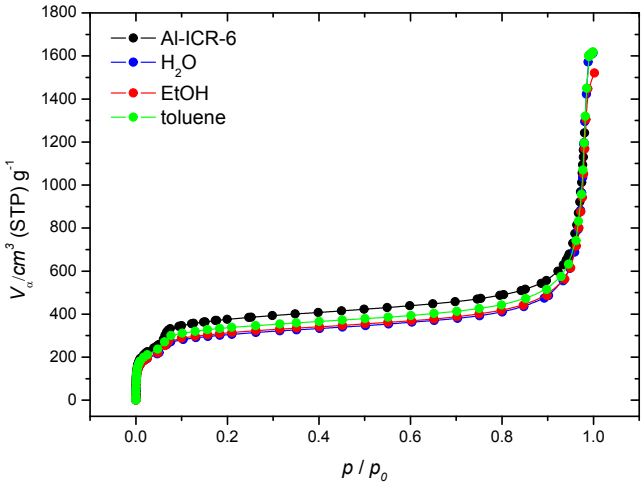

Figure S56. Nitrogen adsorption isotherms of as-synthetized Al-ICR-6 (black) and Al-ICR-6 after 24 h treatment in H_2O, EtOH, and toluene at RT.

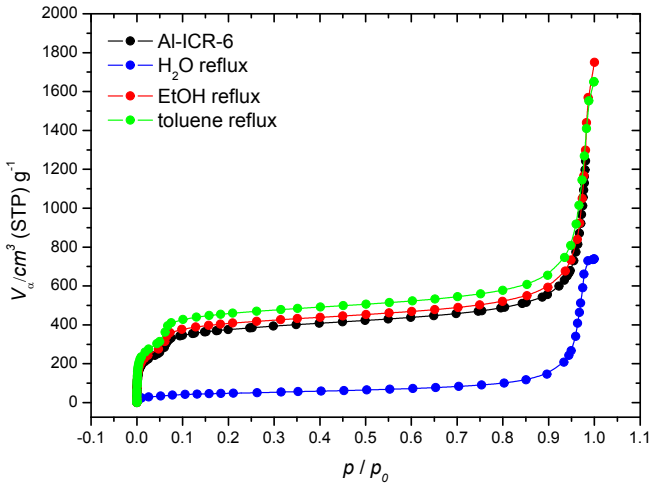

Figure S57. Nitrogen adsorption isotherms of as-synthetized Al-ICR-6 (black) and Al-ICR-6 after 24 h treatment in boiling H_2O, EtOH, and toluene.

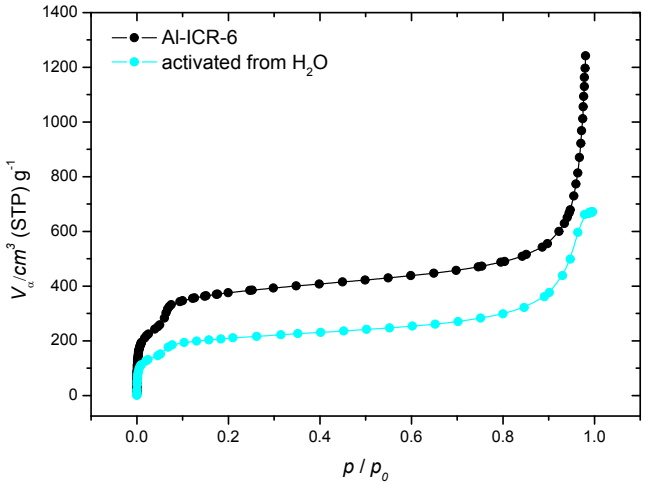

Figure S58. Nitrogen adsorption isotherms of as-synthetized Al-ICR-6 (black) and Al-ICR-6 activated from water.

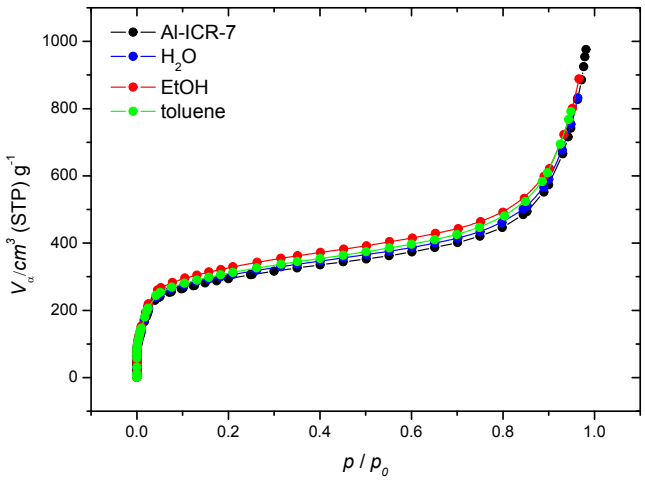

Figure S59. Nitrogen adsorption isotherms of as-synthetized Al-ICR-7 (black) and Al-ICR-7 after 24 h treatment in H_2O, EtOH, and toluene at RT.

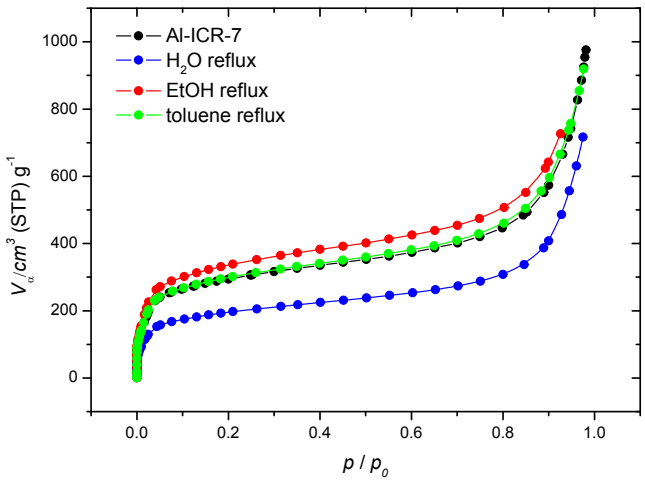

Figure S60. Nitrogen adsorption isotherms of as-synthetized Al-ICR-7 (black) and Al-ICR-7 after 24 h treatment in boiling H_2O, EtOH, and toluene.

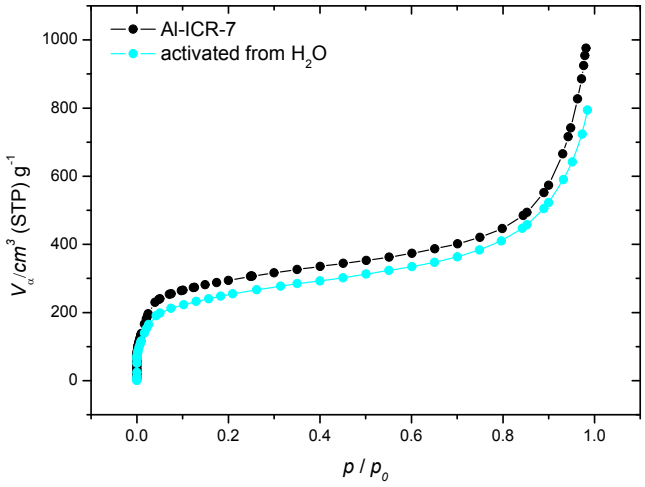

Figure S61. Nitrogen adsorption isotherms of as synthetized Al-ICR-7 (black) and Al-ICR-7 activated from water.

Equations used for the analysis of adsorption properties of ICR MOFs

q_e calculation from HPLC results:

$$q_e = \frac{(C_0 - C_e)\,V}{m} \qquad (1),$$

where q_e is the adsorbed amount of BPA per unit mass of sorbent (mg g^{-1}), C_0 and C_e are initial concentration of BPA (mg L^{-1}) and measured equilibrium concentration of BPA (mg L^{-1}), respectively, V is the total volume (L), and m is the weighted amount of adsorbent (g).

Pseudo-second order kinetic model:

$$q_e = \frac{Q_m^2\, k_2\, t}{1 + k_2 Q_m} \qquad (2),$$

where q_e is calculated using Eq. (1) (mg g^{-1}), Q_m is the amount of BPA adsorbed at the equilibrium (mg g^{-1}), t is time of adsorption (min), and k_2 stands for the pseudo-second order rate constant (g mg^{-1} min^{-1}).[1]

Langmuir model:

$$q_e = \frac{K_L Q_m C_e}{1 + K_L C_e} \qquad (3),$$

where q_e is calculated using Eq. (1), Q_m is the Langmuir maximum sorption capacity (mg g^{-1}), C_e stands for the BPA concentration at the equilibrium (measured, mg L^{-1}), and K_L is the Langmuir constant (L mg^{-1}) which is the measure of the affinity of adsorbate to adsorbent.[5]

Freundlich model:

$$q_e = K_F C_e^{1/n} \qquad (4),$$

where q_e is given by Eq. (1), K_F ([(mg g^{-1}) (mg L^{-1})$^{-n}$]) stands for the Freundlich constant, C_e is the BPA concentration at the equilibrium (mg L^{-1}), and n is a parameter which indicates a degree of surface heterogeneity and is related to the sorption capacity.[5,6]

Langmuir-Freundlich model:

$$q_e = Q_m \frac{K_{LF} C_e^{1/n}}{1 + K_{LF} C_e^{1/n}} \qquad (5),$$

where q_e is calculated using Eq. (1), Q_m is the Langmuir-Freundlich maximum sorption capacity (mg g^{-1}), C_e stands for the BPA concentration at the equilibrium (measured, mg L^{-1}), and K_{LF} (L mg^{-1}) with $1/n$ are the Langmuir-Freundlich constants.[7,8]

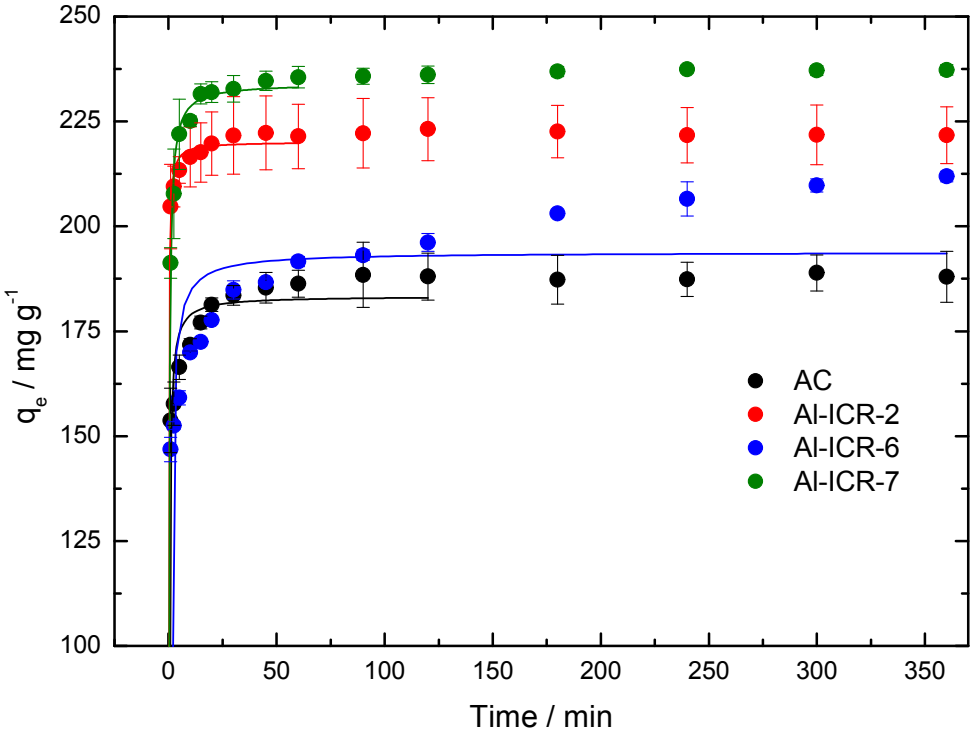

Figure S62. Kinetic curves of BPA adsorption. Dots are experimental points obtained in triplicate experiments and solid lines represent fits to the pseudo-second order kinetic model. The equilibrium points were not used for the fitting (approximately > 100 min) as recommended in literature.1 In the case of Al-ICR-6, the kinetic curve was fitted in entire range because the equilibrium state was not reached within the recorded time.

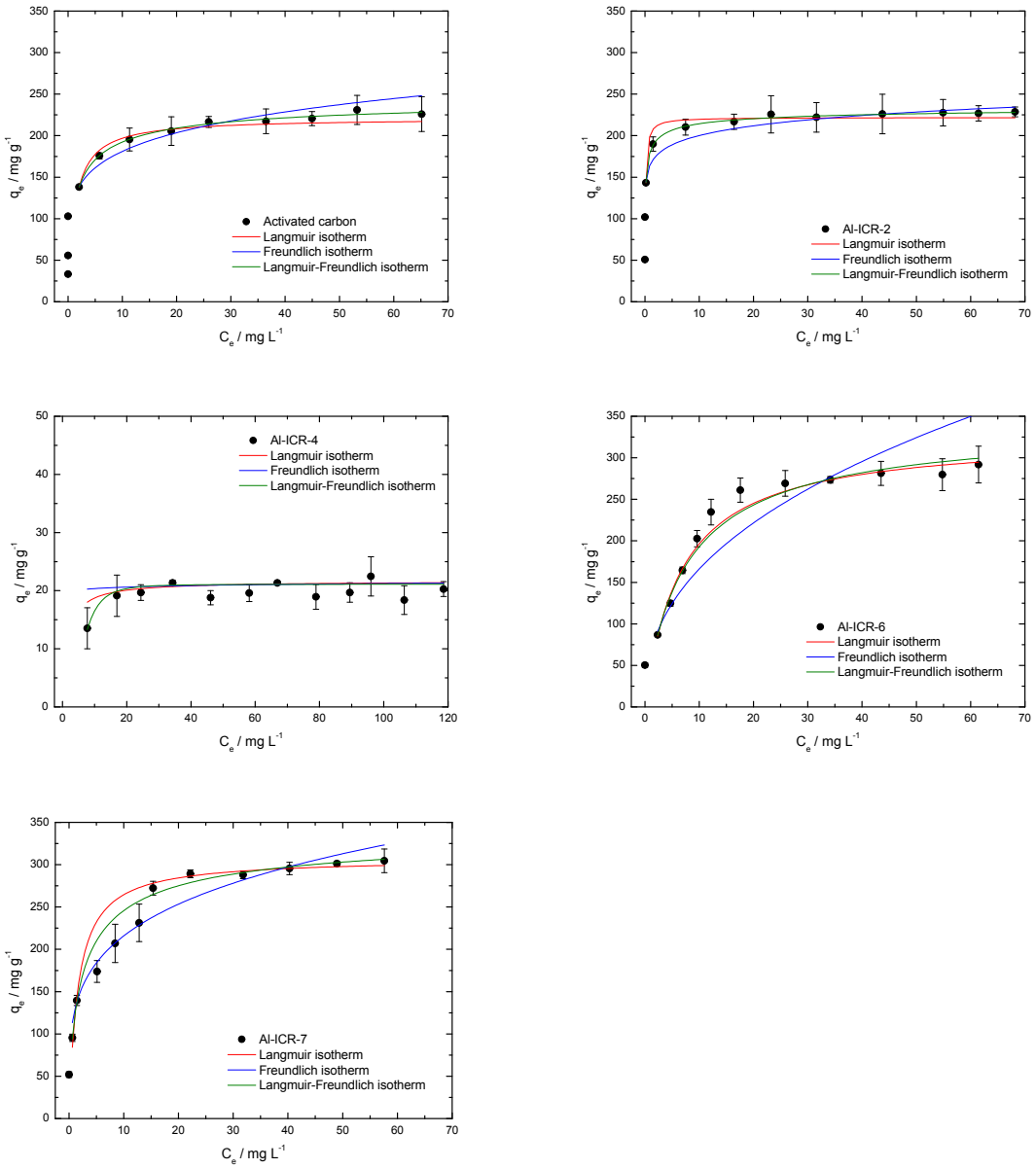

Figure S63. Fitting of isotherms to the Langmuir, Freundlich, and Langmuir-Freundlich adsorption models. Resulting parameters are given in Table S3. Only experimental points with $C_e > 0$ were chosen for the fitting.

Table S3. Langmuir, Freundlich, and Langmuir-Freundlich parameters resulting from the fitting (see Eqs. 1 – 5 for details).

Adsorbent	Kinetic constants			Langmuir constants		
	q_m (mg g^{-1})	k_2 (g mg^{-1} min^{-1})	R^2	Q_m (mg g^{-1})	K_L (L mg^{-1})	R^2
AC	183±2	0.022±0.001	0.987	221±4	0.81±0.04	0.984
Al-ICR-2	220±7	0.052±0.002	0.999	222±3	9.61±0.51	0.981
Al-ICR-4	n. a.	n. a.	n. a.	22±1	0.64±0.58	0.062
Al-ICR-6	194±4	0.010±0.002	0.938	326±8	0.15±0.01	0.993
Al-ICR-7	234±1	0.017±0.002	0.998	307±5	0.62±0.07	0.979

Adsorbent	Freundlich constants			Langmuir-Freundlich constants			
	K_F [(mg g^{-1}) (mg L^{-1})$^{-n}$]	n	R^2	Q_m (mg g^{-1})	K_{LF} (L mg^{-1})	n	R^2
AC	123±2	5.9±0.3	0.962	248±5	0.80±0.10	1.58±0.09	0.999
Al-ICR-2	165±2	12.1±0.6	0.973	239±2	2.28±0.11	3.10±0.17	0.999
Al-ICR-4	20±3	54.9±102	0.068	21±1	0.004±0.02	0.34±0.24	0.181
Al-ICR-6	63±4	2.4±0.1	0.958	340±23	0.15±0.01	1.07±0.10	0.992
Al-ICR-7	127±10	4.3±0.4	0.951	344±21	0.53±0.6	1.47±0.21	0.990

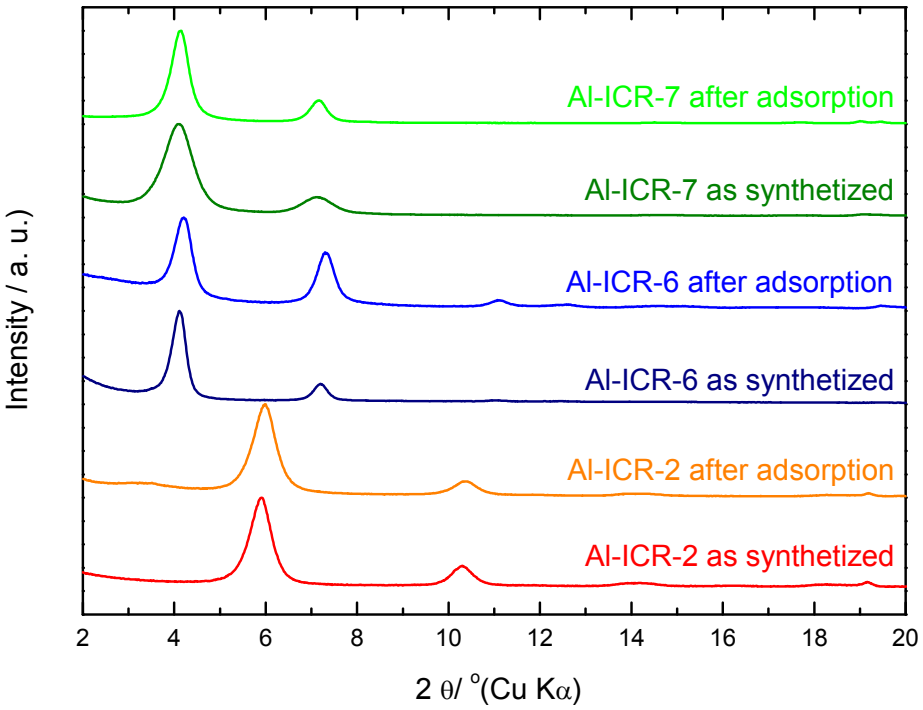

Figure S64. Comparison of the PXRD patterns of Al-ICR MOFs before and after adsorption of BPA and regeneration by acetone. Conditions of adsorption: 10 mg of adsorbent was mixed with 50 mL of BPA solution, initial BPA concentration was 100 mg L^{-1}. The mixture was stirred at constant temperature of 25 °C for 24 h. After the experiment, resulting adsorbent was separated using centrifuge, washed twice by water and three times with acetone. The solid was air-dried overnight, followed by standard activation and PXRD and N_2 adsorption measurement.

Table S4. Comparison of the specific surface areas of Al-ICR MOFs before and after adsorption of BPA and regeneration by acetone.[a]

Adsorbent	**Specific surface area (m^2 g^{-1})**	
	As-synthetized	After adsorption
Al-ICR-2 [b]	933	915
Al-ICR-6 [c]	1362	1041[d]
Al-ICR-7 [c]	1030	980

[a] Conditions of adsorption: 10 mg of adsorbent was mixed with 50 mL of BPA solution, initial BPA concentration was 100 mg L^{-1}. The mixture was stirred at constant temperature of 25 °C for 24 h. After the experiment, resulting adsorbent was separated using centrifuge, washed twice by water and three times with acetone. The solid was air-dried overnight, followed by standard activation and PXRD and N_2 adsorption measurement.

[b] Specific surface area calculated by the t-plot.

[c] BET specific surface area.

[d] The decrease between as-synthetized and after adsorption and regeneration is in line with the decrease observed after shaking in water at RT and therefore is not related to adsorption of BPA.

Details of molecular modelling

Classical molecular simulations were used for evaluation of sorption properties and interactions of BPA with Al-ICR-2, Al-ICR-6, and Al-ICR-7. The MOF supercells were constructed on the bases of their Fe-ICR analogues. The cell parameters were taken from crystallographic data. In the case of Al-ICR-2 we created the 1a x 2b x 3c supercell, and for Al-ICR-6 and Al-ICR-7 we created 2a x 2b x 3c supercells, all containing 4 pores. Free volume within the pores was calculated using water molecule as a probe with a radius of 1.44 Å (weighed average of the van der Waals radii taken from the Dmol3 program implemented in the Materials Studio software: 1.72 Å for oxygen and 1.3Å for hydrogen).[9] Each pore was filled with corresponding amount of water (100, 312, and 250 water molecules for Al-ICR-2, Al-ICR-6, and Al-ICR-7, respectively). Then, BPA molecules were placed into each pore (8 water molecules were replaced by one BPA). Since experimental measurements revealed high concentrations of BPA adsorbed in the MOF structures, we carried out the calculations in the following way: First, we created models containing single BPA (adsorbed amount $q_e \approx 10$ mg g^{-1}) in the centre of each pore to find its binding sites and explore its behaviour at low concentrations. Then, we created models containing amounts of BPA corresponding to $q_e \approx$ 100, 200, and 300 mg g^{-1}. For Al-ICR-2, we created only two models containing 7 or 14 BPA molecules per supercell (corresponding to $q_e \approx 100$ and 200 mg g^{-1}) because higher concentrations of BPA were not experimentally observed.

In the case of Al-ICR-6 and Al-ICR-7, the BPA loadings selected for $q_e \approx 100$, 200, and 300 mg g^{-1}, i.e., 10, 20, or 31 BPA molecules per supercell of Al-ICR-6 and 14, 28, or 40 BPA molecules per supercell of Al-ICR-7. The initial positions of BPA molecules were practically the same and close to the positions obtained in the simulations containing single BPA molecule in each pore.

The geometry of all initial models was optimized and subsequent molecular dynamics simulations in an NVT statistical ensemble at 300 K were carried out in the LAMMPS simulation package.[10] One dynamic step was 1 fs and $5 \cdot 10^6$ steps were carried out. The snapshots were collected every 10 ps and the snapshots of the last 1.5 ns were used for the analyses. The charges of all MOFs were calculated using the Qeq method[11] and all the simulations were performed using the pcff forcefield.[12] The electrostatic interactions were calculated using the PPPM method, van der Waals interactions were calculated using the Lennard-Jones potential with a cut-off distance of 12 Å. In all cases, the atomic positions in the structures were kept fixed and the atomic positions of other atoms were variable.

The pores of ICR MOFs are not smooth. The organic linkers in Al-ICR-6 and Al-ICR-7 form grooves whose dimensions approximately corresponds to the size of biphenyl (length and width of 7 and 5 Å, respectively).

Figure S65 shows snapshots of two stable arrangements of BPA molecules in the Al-ICR-6 pore containing a single molecule in each pore ($q_e \approx 10$ mg g^{-1}). The first position is characteristic by the placement of BPA methyl groups above the groove with the OH substituents aiming into the pore and one phenyl ring approximately parallel with the nearest phenyl ring of the pore wall (Figure S65a,b). The second position is characterized by a close contact of the pore wall and the BPA methyl groups (approximately 2.6 Å in average measured between the nearest H atoms), and the connecting line of BPA OH substituents is approximately perpendicular to the pore axis (Figure S65c,d). The interaction energy between BPA and the Al-ICR-6 structure is of -19.1 kcal mol^{-1} in average for the first position (Figure S65a,b) and of -22.0 kcal mol^{-1} in average for the second position (Figure S65c,d). The BPA molecule changes these two positions during the simulations.

The situation is different in Al-ICR-7. The BPA molecule has a tendency to adopt a close contact with the pore wall similarly to Al-ICR-6, but the presence of bulky phenyls makes such contact impossible. These sterical reasons lead to a larger distance between the pore wall and BPA molecule (Figure 5c). Then, the interaction energy is -18.2 ± 0.4 kcal mol^{-1}, indicating that BPA has higher affinity to Al-ICR-6 at low concentrations.

The pore diameter of Al-ICR-2 is significantly smaller than the pores in Al-ICR-6 and Al-ICR-7. A possible orientation of single BPA molecule within the Al-ICR-2 pore is shown in Figure 5a. The size similarity of BPA molecule and the pore causes that the interaction energy of -22.2 ± 0.4 kcal mol^{-1} is the strongest of all investigated ICR MOFs, indicating that Al-ICR-2 is the best sorbent at low BPA concentrations ($q_e \approx 10$ mg g^{-1}).

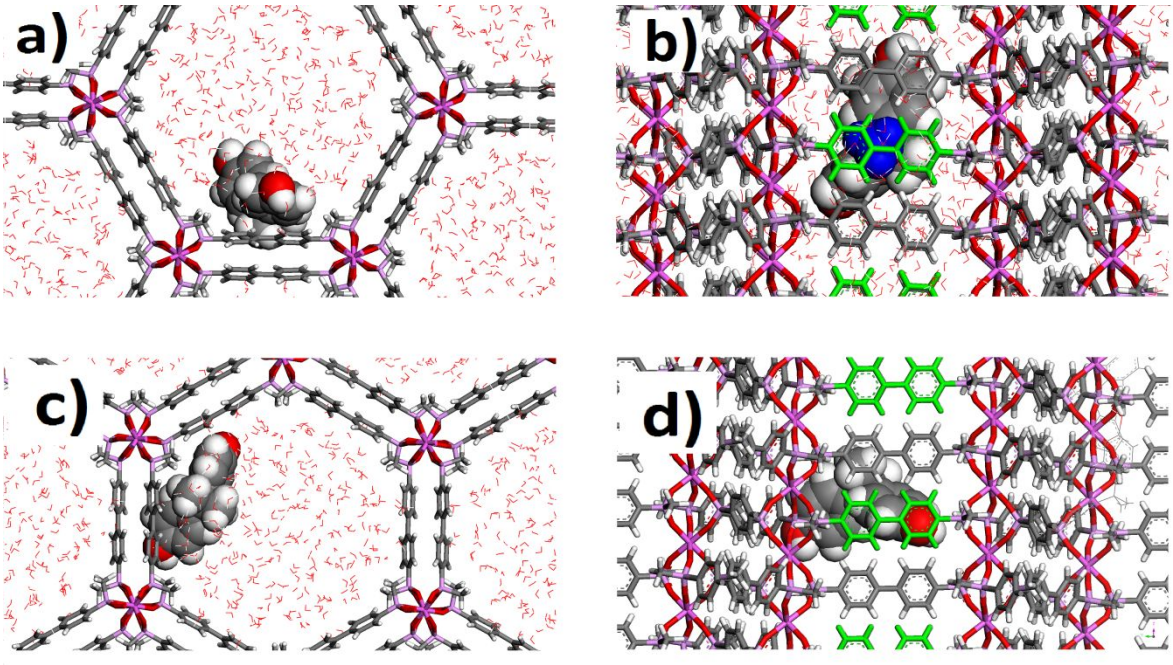

Figure S65. Detailed view on the BPA arrangement inside the Al-ICR-6 pores along the pore axis (left) and in the perpendicular direction to the pore axis (right). The biphenyl rings in green are in the front and represent the bottom of the groove, methyl groups of BPA are in blue and oxygen atoms are in red.

The BPA arrangement depends on the saturation of the pores. Figure S66 shows the arrangement of BPA along the pore axis for $q_e \approx 300$ mg g^{-1} to visually compare the free pore volumes of Al-ICR-6 and Al-ICR-7. The free volume after removing all water molecules is 74 % for Al-ICR-6 and 58 % for Al-ICR-7. If we take into account the absolute values of free volume of Al-ICR-6 and Al-ICR-7, the free volume of Al-ICR-6 is about 50 % larger than in the case of Al-ICR-7. The lower free volume of Al-ICR-7 leads to a more difficult penetration of other BPA molecules into the pores and theoretically to a lower sorption capacity under the same conditions.

Based on the simulation results we can conclude that the presence of different linkers can tune the host-guest interactions especially for low q_e values of BPA. With increasing BPA concentrations the effects of linker sizes on the host-guest interactions gradually diminish and maximal sorption capacity is given mainly by the free pore volume of ICR MOF.

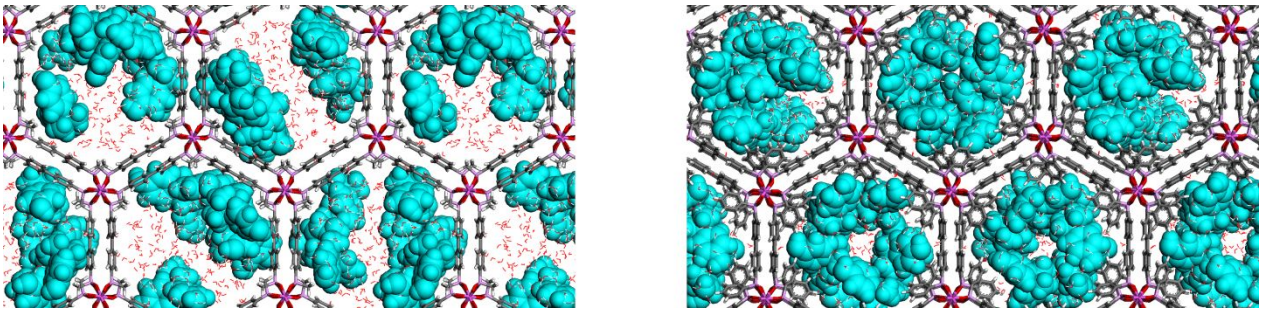

Figure S66. Arrangement of BPA molecules with a loading of approximately 300 mg g^{-1} in the pores of Al-ICR-6 (left) and Al-ICR-7 (right).

References

[1] Simonin, J.-P. On the Comparison of Pseudo-First Order and Pseudo-Second Order Rate Laws in the Modeling of Adsorption Kinetics. *Chem. Eng. J.*, **2016**, *300*, 254-263.

[2] Palatinus, L.; Chapuis, G. Superflip - a Computer Program for the Solution of Crystal Structures by Charge Flipping in Arbitrary Dimensions. J. Appl. Cryst. 2007, 40, 786-790.

[3] J. Rohlícek, M. Husák, MCE2005 - a new version of a program for fast interactive visualization of electron and similar density maps optimized for small molecules. J. Appl. Cryst. **2007**, *40*, 600-601.

[4] Hynek, J.; Brázda, P.; Rohlíček, J.; Londesborough, M. G. S.; Demel, J. Phosphinic Acid Based Linkers: Building Blocks in Metal–Organic Framework Chemistry. *Angew. Chem. Int. Ed.* **2018**, *57*, 5016 –5019.

[5] Foo, K. Y.; Hameed, B. H. Insight into the Modeling of Adsorption Isotherm Systems. *Chem. Eng. J.*, **2010**, *156*, 2-10.

[6] Kecili, R.; Hussain, Ch. M. Mechanism of Adsorption on Nanomaterials. Nanomaterials in Chromatography, 2018, Chapter 4, 89-115.

[7] Wang, S.; Vincent, T.; Faur, C.; Guibal E. A Comparison of Palladium Sorption Using Polyethylenimine Impregnated Alginate-Based and Carrageenan-Based Algal Beads. *Appl. Sci.* **2018**, *8*, 264-281.

[8] Jeppu, G. P.; Clement. T. P. A Modified Langmuir-Freundlich Isotherm Model for Simulating pH-Dependent Adsorption Effects. *J. Contam. Hydrol.*, **2012**, *129–130*, 46–53.

[9] Materials Studio Modeling Environment, Release 4.3 Documentation. Accelrys Software Inc., San Diego, CA, 2003.

[10] Plimpton, S. Fast Parallel Algorithms for Short-Range Molecular Dynamics. *J. Comput. Phys.* **1995**, *117*, 1-19

[11] Rappe, A. K.; Goddard III, W. A. Charge Equilibration for Molecular Dynamics Simulations. *J. Phys. Chem.* **1991**, *95*, 3358-3363.

[12] Sun, H.; Mumby, S. J.; Maple, J. R.; Hagler. A. T. An ab Initio CFF93 All-Atom Force Field for Polycarbonates. *J. Am. Chem. Soc.* **1994**, *116*, 2978–2987.